Small-Angle X-ray Scattering by Nanostructured Materials

39

Aldo F. Craievich

Contents

A. F. Craievich (✉)
Institute of Physics, University of São Paulo, São Paulo, Brasil
e-mail: craievich@if.usp.br

L. Klein et al. (eds.), *Handbook of Sol-Gel Science and Technology*,
https://doi.org/10.1007/978-3-319-32101-1_37

Abstract

This chapter contains the basic theory of small-angle X-ray scattering (SAXS) and its applications to low-resolution studies of nanostructured materials. The primary purpose is to explain how to obtain structural information from simple systems whose low-resolution structure can be described by a two-electron density model, consisting of either homogeneous nanoparticles embedded in a (solid or liquid) medium with constant electron density or two-phase bicontinuous systems. The presented SAXS theory and the examples of applications refer to different procedures for determinations of geometrical parameters associated to nanoparticles or clusters in dilute solution, spatially correlated nanoparticles, and more general two-phase systems, namely, particle radius of gyration, interface area, size distribution, fractal dimension, and interparticle average distance. Other described applications are in situ SAXS studies of mechanisms involved in transformation processes leading to nanostructured materials such as those occurring in nanophase separation and along the successive steps of sol-gel routes. One section is dedicated to present the basic concepts and describes an application of grazing incidence small-angle scattering (GISAXS), which allows for studying nanostructured thin films and thin layers located close to the external surface of solid substrates. Most of the reported applications refer to nanostructured materials obtained by sol-gel processing and are based on experimental results published by the author and collaborators.

Introduction

This chapter describes the basic theory of small-angle X-ray scattering (SAXS) and reports a number of examples of application of this experimental technique to low-resolution structural investigations. Several examples also show how SAXS is applied to the characterization of transformation mechanisms in different nanomaterials.

Sol-gel processing starts from colloidal particles in liquid solution and often leads to solid materials with interesting properties. Along all steps of sol-gel transformations the nanoscopic nature of the structure is preserved. This chapter includes several applications of SAXS technique to in situ characterizations of precursor systems starting from liquid sols up to final solid nanostructured materials.

The basic process of the scattering of X-rays by materials is the photon–electron interaction. As it will be seen along this chapter, the complex amplitude (or modulus and phase) of the electromagnetic wavelets associated to photons elastically scattered in all directions by any material, is related to the tridimensional electron density function $\rho\left(\vec{r}\right)$ through a Fourier transformation.

The electron density function $\rho\left(\vec{r}\right)$ fully describes the structure of materials; thus the ultimate goal of crystallographers and materials scientists is to determine this function, starting from experimental X-ray scattering patterns. Although this detailed information is not in practice fully obtained, relevant and useful structural features can generally be inferred.

A typical SAXS setup is schematically shown in Fig. 1a. This technique provides useful structural information about heterogeneities in electron density sized within the range ~5 to 500 Å, these limits depending on the photon energy, sample-to-detector distance, size of the beam-stopper and geometry of the X-ray detector. Very large objects as compared to the X-ray wavelength (with a size above, say, 1 μm) produce noticeable scattering intensity only within an extremely small angular

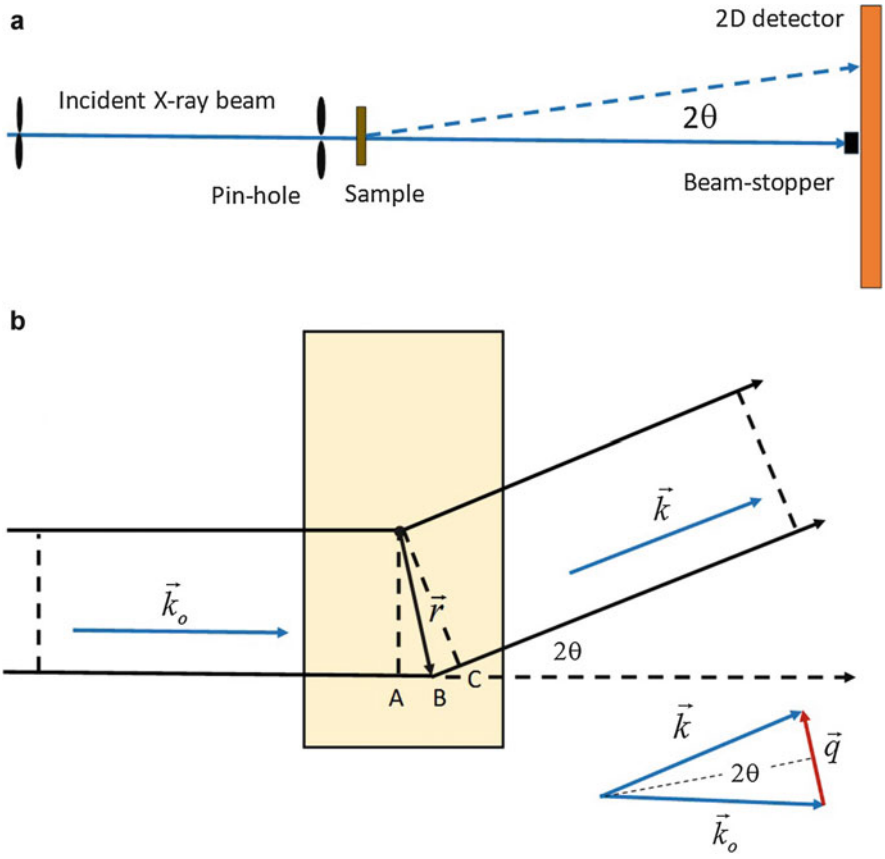

Fig. 1 (**a**) Schematic SAXS setup. (**b**) X-ray beam paths from the source (*left*) to the detector (*right*), both located far away from the sample. The total segment $\Delta s = \overline{AB} + \overline{BC}$ is the optical path difference associated to the X-ray scattering by electrons in two elements of volume $d\vec{r}$, from which the phase shift is determined

domain close to the direction of the incident beam. Thus in this case the scattered photons hit the incident beam-stopper and are not recorded by the X-ray detector.

Notice that the X-ray scattering intensity patterns within the "small-angle" range do not contain any information about the very short wavelength modulations in electron density associated to the atomic nature of the material, the effects from them only appearing in the scattering intensity profiles recorded at wide angles.

Basic Theory

General Equations

The intensity associated to electromagnetic waves elastically scattered by an electron was derived by Thompson. Since the amplitude of the X-ray wave scattered by an electron has a well-defined phase relation with the amplitude of the incident wave, interference between scattered wavelets occurs. For a nonpolarized incident X-ray beam with intensity I_0, the intensity associated to the wavelets scattered by one electron per unit solid angle Ω, is $I_e(2\theta) = I_0[(1 + \cos^2 2\theta)/2].r_e^2$, where 2θ is the scattering angle (i.e., the angle between the wave-vectors of incident and scattered photons), and r_e is the classical electron radius. The X-ray intensity associated to the elastic scattering by an electron at small angles per unit of incident beam intensity and per unit of solid angle can be considered as a constant, $I_e = r_e^2$. Using this approximated value, the relative error in I_e for 2θ up to 8° is <1%.

In addition to coherent elastic X-ray scattering, electrons also produce inelastic Compton scattering. Since in Compton scattering there is no phase relationship between incident and scattered waves, the scattered wavelets do not interfere, and thus the total scattering intensity is not modulated by structural effects. On the other hand, since the intensity of Compton scattering within the small angle range is weak, its contribution is in practice neglected.

Let us now consider an incident monochromatic and narrow X-ray beam with wave-vector $\vec{k}_0$ hitting a material with an arbitrary structure defined by its electron density function $\rho\left(\vec{r}\right)$ and a generic scattering direction defined by the wave-vector $\vec{k}$, as shown in Fig. 1b. Since Thompson scattering is an elastic interaction, the moduli of $\vec{k}_0$ and $\vec{k}$ are both equal to $2\pi/\lambda$, λ being the X-ray wavelength.

The contribution from each volume element to the total amplitude of the scattered wave in a direction defined by the wave-vector $\vec{k}$ is equal to the amplitude of the wavelet scattered by one electron, A_e, multiplied by the number of electrons in the volume element $d\vec{r}$ and by a factor that accounts for the effect of phase shift $\Delta\varphi$, i.e., $dA = A_e\rho\left(\vec{r}\right)d\vec{r}\ e^{i\Delta\varphi}$. Thus the total scattering amplitude is the integral over the whole sample volume V of the electron density function multiplied by a phase factor $e^{i\Delta\varphi}$.

The difference in optical paths Δs associated to two wavelets corresponding to the scattering by electrons contained in two volume elements as shown in Fig. 1b is equal to $\overline{AB} + \overline{BC}$. Thus the phase shift is $\Delta\varphi = 2\pi\left(\overline{AB} + \overline{BC}\right)/\lambda$ or, equivalently, $\Delta\varphi = -\left(\vec{k}.\ \vec{r} - \vec{k}_0.\ \vec{r}\right)$. Defining the so-called scattering vector as $\vec{q} = \vec{k} - \vec{k}_0$, the phase shift becomes $\Delta\varphi = -\ \vec{q}\ .\ \vec{r}$. Thus the total scattering amplitude associated to the whole sample volume V is

$$A\left(\vec{q}\right) = \int_V \rho\left(\vec{r}\right) e^{-i.\vec{q}.\vec{r}}\, d\vec{r} \tag{1}$$

Since the scattering amplitude A_e and scattering intensity $I_e = |A_e|^2$ appear as a factor many times along this chapter, in Eq. 1 and in further equations I_e and A_e are set equal to 1 for brevity.

As it can be verified in Fig. 1b, the modulus of the scattering vector $\vec{q}$ is $q = (4\pi/\lambda)\sin\theta$, θ being half the scattering angle. Since $\sin\theta \approx \theta$ for small angles, the modulus of the scattering vector in SAXS experiments is approximately proportional to the scattering angle.

Equation 1 yields the amplitude of the scattered waves under the assumptions of the kinematical theory of X-ray scattering, disregarding multiple scattering and absorption effects (Guinier and Fournet 1955). Equation 1 implies that the total amplitude $A\left(\vec{q}\right)$ is the Fourier transform of the electron density function $\rho\left(\vec{r}\right)$. Consequently, the electron density $\rho\left(\vec{r}\right)$ can be determined by inverse Fourier transformation of the function $A\left(\vec{q}\right)$:

$$\rho\left(\vec{r}\right) = \frac{1}{(2\pi)^3}\int A\left(\vec{q}\right) e^{i.\vec{q}.\vec{r}}\, d\vec{q} \tag{2}$$

The function $A\left(\vec{q}\right)$ corresponds to the amplitude of the scattered waves defined in the reciprocal or Fourier space ($\vec{q}$ space). Notice that the amplitude $A\left(\vec{q}\right)$ is a complex function specified by its real and imaginary parts or, alternatively, by its modulus and phase.

Taking into account the mathematical properties of Fourier transformation, the electron density $\rho\left(\vec{r}\right)$, which defines the *high-resolution* material structure (i.e., the precise atomic configuration), can be determined only if the complex function $A\left(\vec{q}\right)$ is known over a large volume in $\vec{q}$ space. On the other hand, if the amplitude $A\left(\vec{q}\right)$ is determined within a small volume in $\vec{q}$ space close to $\vec{q} = 0$ (i.e., at small scattering angles), Eq. 2 only yields the *low-resolution* features of the structure.

A fundamental difficulty arises in the analysis of results of scattering experiments because usual X-ray detectors count photons, i.e., what is experimentally determined is the scattering intensity $I\left(\vec{q}\right)$ and not the modulus and phase of the amplitude $A\left(\vec{q}\right)$. Since $I\left(\vec{q}\right) = A\left(\vec{q}\right) \cdot A\left(\vec{q}\right)^* = \left|A\left(\vec{q}\right)\right|^2$, the square root of the measured $I\left(\vec{q}\right)$ function yields the modulus of the scattering amplitude $\left|A\left(\vec{q}\right)\right|$, its phase remaining unknown. Thus Eq. 2 cannot directly be applied to determine the electron density function $\rho\left(\vec{r}\right)$. This is the known *phase problem* that crystallographers and materials scientists face when they try to determine atomic structures from results of X-ray scattering experiments.

Since the phase of the scattering complex amplitude $A\left(\vec{q}\right)$ cannot be experimentally determined, it seems useful to establish which is the function related to the structure and defined in the direct space that can be obtained by inverse Fourier transformation of the experimental scattering intensity $I\left(\vec{q}\right)$.

The electron density $\rho\left(\vec{r}\right)$ can be written as an average density ρ_a plus local deviations defined by $\Delta\rho\left(\vec{r}\right)$, so as $\rho\left(\vec{r}\right) = \rho_a + \Delta\rho\left(\vec{r}\right)$. By substituting $\rho\left(\vec{r}\right)$ in Eq. 1, the scattering amplitude becomes

$$A\left(\vec{q}\right) = \int_V \rho_a e^{-\vec{q}\cdot\vec{r}}\, d\vec{r} + \int_V \Delta\rho\left(\vec{r}\right) e^{-\vec{q}\cdot\vec{r}}\, d\vec{r} \tag{3}$$

For a macroscopic sample with a volume V and large dimensions compared to the X-ray wavelength, the first integral yields nonzero values only over an extremely small q range close to $q = 0$, which is not reached in typical SAXS experiments. Thus, the scattering intensity, $I\left(\vec{q}\right) = A\left(\vec{q}\right).A\left(\vec{q}\right)^*$ over the accessible $\vec{q}$ range is given by

$$I\left(\vec{q}\right) = \int_V \int \Delta\rho\left(\vec{r}_1\right) \Delta\rho\left(\vec{r}_2\right) e^{-\vec{q}\cdot\left(\vec{r}_1 - \vec{r}_2\right)} d\vec{r}_1 d\vec{r}_2 \tag{4}$$

Putting $\vec{r}_1 - \vec{r}_2 = \vec{r}$, Eq. 4 becomes

$$I\left(\vec{q}\right) = V \int_V \gamma\left(\vec{r}\right).e^{-\vec{q}\cdot\vec{r}}\, d\vec{r} \tag{5}$$

where

$$\gamma\left(\vec{r}\right) = \frac{1}{V}\int_V \Delta\rho\left(\vec{r}'\right)\Delta\rho\left(\vec{r}' + \vec{r}\right) d\vec{r}' = \left\langle \Delta\rho\left(\vec{r}'\right)\Delta\rho\left(\vec{r}' + \vec{r}\right)\right\rangle \tag{6}$$

the symbol $< >$ indicating the average over the analyzed sample volume V.

As indicated by Eq. 6 the function $\gamma\left(\vec{r}\right)$ – named correlation function (Debye and Bueche 1949) – is the volume average of the product of $\Delta\rho$ in two volume elements connected by the vector $\vec{r}$. The correlation function $\gamma\left(\vec{r}\right)$ is determined from the experimental scattering function $I\left(\vec{q}\right)$ by inverse Fourier transformation:

$$\gamma\left(\vec{r}\right) = \frac{1}{(2\pi)^3 V}\int I\left(\vec{q}\right)e^{i\vec{q}\cdot\vec{r}}\,d\vec{q} \tag{7}$$

Provided that $\rho\left(\vec{r}\right)$ is known, the correlation function $\gamma\left(\vec{r}\right)$ can be determined by applying Eq. 6. But, inversely, from a known $\gamma\left(\vec{r}\right)$ function, $\rho\left(\vec{r}\right)$ cannot be unambiguously inferred.

For isotropic systems, the correlation function is independent of the direction of the vector $\vec{r}$, i.e., $\gamma\left(\vec{r}\right)$ becomes $\gamma(r)$ and, consequently, the scattering intensity, $I(q)$, is also isotropic. For isotropic systems the function $e^{-i\vec{q}\cdot\vec{r}}$ is replaced in Eq. 5 by its spherical average $\left\langle e^{-i\vec{q}\cdot\vec{r}}\right\rangle_{\Omega} = \sin qr/qr$. Thus Eqs. 5 and 7, respectively, become

$$I(q) = V\int_0^\infty 4\pi r^2\gamma(r)\frac{\sin qr}{qr}\,\mathrm{d}r \tag{8}$$

$$\gamma(r) = \frac{1}{(2\pi)^3 V}\int_0^\infty 4\pi q^2 I(q)\frac{\sin qr}{qr}\,\mathrm{d}q \tag{9}$$

A useful procedure that is often applied to characterize low-resolution structures, circumventing the phase problem, is to begin with an initial model described by a guessed electron density function $\rho\left(\vec{r}\right)$. The scattering amplitude is thus determined by using Eq. 1 and then the resulting scattering intensity $I\left(\vec{q}\right) = |A\left(\vec{q}\right)|^2$ is compared to the experimental intensity function. The use of ad hoc computer programs allows for many iterations and modifications of the structure model, until a good fit of the calculated function to the experimental curve is achieved. This procedure is, for example, applied to the determination of low-resolution structures (envelope functions) of proteins in dilute solution (Svergun 1999).

For materials consisting of isolated (in general nonidentical) nanoparticles embedded in a homogeneous matrix, the scattering intensity $I(q)$ is often modeled under the assumption of simple shapes and taking also into account eventual effects from spatial correlation. The model function is then fitted to the experimental scattering curves. An eventual good fitting justifies a posteriori the proposed model and yields the adjusted parameters that characterize the structure of the studied material.

In another procedure, which is often applied to study structural transformations in materials subjected to isothermal annealing, the isotropic correlation function $\gamma(r)$ is theoretically determined starting from basic thermodynamic and/or statistical concepts (Cahn 1965; Lebowitz et al. 1982). This is followed by the determination of $I(q)$ for increasing periods of time using Eq. 8 and further comparison of the series of model functions with the sequence of experimental SAXS curves determined in situ along the structural transformation. This procedure is applied, for example, to verify the correctness of theoretical models of particle growth and structure coarsening.

Small-Angle Scattering by Nanoscopic Two-Phase Systems: Porod's Law

This section deals with isotropic biphasic materials, i.e., isotropic two-electron density systems with sharp interfaces, such as those schematically drawn in Fig. 2a, b. In this model the relevant parameters are the electron densities ρ_1 and ρ_2 and the volume fractions φ_1 and $\varphi_2=1-\varphi_1$. This model is applied to characterize different nanostructured materials such as nanoporous solids, nanocrystals, or disordered nanoclusters embedded in solid or liquid media, etc.

The general properties of Fourier analysis tell us that the asymptotic trend, at high q, of the scattering intensity $I(q)$ is connected to the behavior of the $\gamma(r)$ function at small r. For isotropic two-electron density systems, the correlation function $\gamma(r)$ can be approximated at small r by (Porod 1982):

$$\gamma(r) = (\rho_1 - \rho_2)^2 \varphi_1 (1 - \varphi_1) \left[1 - \frac{S}{4V\varphi_1(1-\varphi_1)} r\right] \tag{10}$$

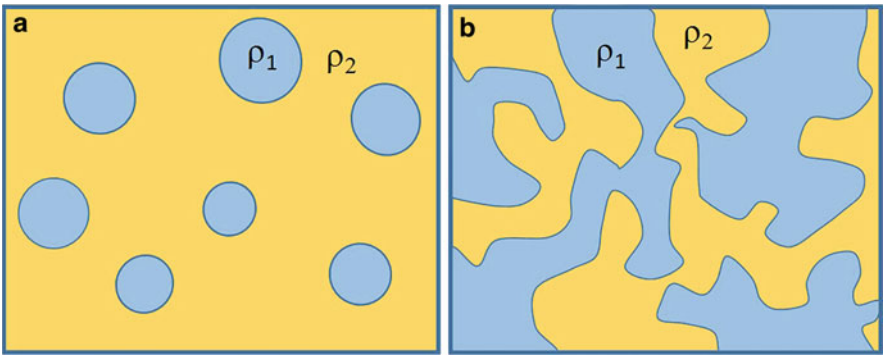

Fig. 2 Schematic examples of two types of biphasic structures or two-electron density systems. (**a**) Set of isolated spherical nano-objects with a constant electron density ρ_1 embedded in a homogeneous matrix with electron density ρ_2. (**b**) Bicontinuous structure, both phases with constant electron densities ρ_1 and ρ_2

where S/V *is* the area of the interface per unit sample volume. Replacing $\gamma(r)$ given by Eq. 10 in Eq. 8 and solving the integral, the leading term of the asymptotic intensity $I(q)$, at high q, is given by (Porod 1982)

$$I(q) = \frac{2\pi(\rho_1 - \rho_2)^2 S}{q^4} \qquad (q \to \infty) \tag{11}$$

Equation 11, named Porod law, applies to isotropic two-electron density systems with sharp interfaces, such as disordered porous materials and other two-phase systems whose relevant structural feature is their interface surface area.

Porod's law applies to either dilute or concentrated systems of isolated nano-objects, provided they are not very thin sheets or very narrow cylinders, for which the asymptotic intensities are proportional to $1/q^2$ and to $1/q$, respectively (Shull and Roess 1947). Equation 11 does not hold for sets of identical spherical or cylindrical nano-objects, because in these cases the SAXS intensity exhibits oscillations even at very high q. By analyzing the features of such oscillations, it is possible to determine the distance between the parallel portions of the interfaces (Ciccariello 1991). However, if the spherical or cylindrical nano-objects have a wide size distribution, the oscillations smear out and the asymptotic Porod's law holds. For anisotropic two-electron density systems, Porod's law still applies along all $\vec{q}$ directions, but the parameter S in Eq. 11 has a different meaning (Ciccariello et al. 2002).

The behavior of $I(q)$ at high q is often analyzed using $I(q)q^4$ vs. q^4 plots. Equation 11 implies that $I(q)q^4$ becomes asymptotically constant in the high-q limit but, for many materials, the SAXS intensity also contains an additional and q-independent contribution from short-range density fluctuations in their phases (Ruland 1971). For these materials, the asymptotic $I(q)q^4$ vs. q^4 plot, at high q, is expected to exhibit a linear dependence (i.e., $I(q)q^4 = a + b\ q^4$) with a positive slope (b > 0). Extrapolation of the linear portion of the $I(q)q^4$ function toward $q^4 = 0$ yields $I(q)q^4(q = 0) = a$. By substituting this value in Eq. 11, the interface area between both phases, S, is determined. On the other hand, Ruland (1971) demonstrated for two-phase systems with a smooth transition in electron density between both phases, that the asymptotic $I(q)q^4$ vs. q^4 plot at high q also exhibits linear dependence but in this case the slope is negative (b < 0).

From Eq. 9 it can be verified that $\gamma(0) = Q/(2\pi^2 V)$, where Q is the integral defined as $Q = \int_0^\infty q^2.I(q)dq$. On the other hand, for two-electron density systems, γ(0) is equal to $(\rho_1 - \rho_2)^2\varphi_1(1 - \varphi_1)$ (Eq. 10), so as the integral Q becomes`

$$Q = \int_0^\infty q^2 I(q)dq = 2\pi^2(\rho_1 - \rho_2)^2 V\varphi_1(1 - \varphi_1) \tag{12}$$

The integral Q depends on the electron density contrast factor $(\rho_1 - \rho_2)^2$ and volume fractions of both phases but not on the specific features of their geometrical

configuration. For example, along structural transformations that preserve both electron densities and phase volume fractions, even though the structure and, consequently, the shape of the scattering intensity curves change, the integral Q is expected to remain constant. Therefore, the integral Q is named "Porod invariant." Examples of transformations that occur without significantly affecting the value of the integral Q are the processes of growth of homogeneous nanoclusters by mechanisms of coarsening or coalescence.

For the determination of the interface surface area S by applying Eq. 11 the measurement of the scattering intensity in absolute units is required (See "Appendix: Experimental Issues"). Moreover, from Eqs. 11 and 12, the following equation is derived:

$$\frac{S}{V} = \pi.\varphi_1(1-\varphi_1)\frac{[I(q)q^4]_{q\to\infty}}{Q} \tag{13}$$

Thus, if the scattering intensity is only known in relative scale and provided the phase volume fractions are known, Eq. 13 allows for the determination of the specific interface surface area (S/V). Equation 13 is often applied to powdered samples, for which the precise measurement of the scattering intensity in absolute units is difficult.

Small-Angle Scattering by Spatially Uncorrelated Nanoparticles: Guinier's Law

The wavelets associated to the X-ray scattering by a dilute set of spatially uncorrelated nano-objects do not interfere. Under this condition and provided the objects are identical and centrosymmetric, the total scattering intensity $I(q)$ is expressed as

$$I(q) = NI_1(q) \tag{14}$$

where N is the number of nanoparticles and $I_1(q)$ is the SAXS intensity produced by a single nanoparticle.

By solving Eq. 8 for an arbitrary correlation function $\gamma(r)$ associated to a single nano-object, it can be demonstrated (Guinier and Fournet 1955) that the SAXS intensity at small q is given by

$$I(q) = N(\Delta n)^2 e^{-R_g^2 q^2/3} (q \to 0) \tag{15}$$

where Δn is the excess in number of electrons inside the nano-objects and R_g their radius of gyration. For nano-objects with volume V_1 and constant electron density ρ_1, embedded in a homogeneous matrix with electron density ρ_2, the number of electrons in excess is $\Delta n = (\rho_1 - \rho_2)V_1$ and the radius of gyration is

$$R_g = \left(\int_{V_1} r^2 d\vec{r} / V_1 \right)^{1/2} \tag{16}$$

Equation 15 is named Guinier law.

In order to derive the radius of gyration R_g of nano-objects from results of SAXS measurements, the Guinier plot (*log I* vs. q^2) is applied. In this plot, a straight line is expected to be observed at small q, within a more or less wide q range depending on the size and shape of the objects (Guinier and Fournet 1955). From the slope α_G of the straight line in Guinier plots, the radius of gyration is determined; $R_g = [3(-\alpha_G/\log.e)]^{1/2} = 2.628.|\alpha_G|^{1/2}$. For example, the radius of gyration of homogeneous spherical objects is related to their radius R by $R_g = (3/5)^{1/2}R$ and that of homogeneous cylinders with radius R and height H by $R_g = \left[\left(R^2/2\right) + \left(H^2/12\right)\right]^{1/2}$. Guinier plots are also applied to determine the SAXS intensity at $q = 0$, $I(0)$, by linear extrapolation of *log I* (q^2) to $q^2 = 0$.

The total SAXS intensity produced by a *dilute* set of nano-objects with a distribution of radii of gyration $N(R_g)$ is given by the sum of the individual contributions of each object. For this system Guinier's law also holds but the derived parameters are weighted averages. For example, for two-electron density systems consisting of a isotropic and polydisperse set of N spatially uncorrelated nano-objects, Eq. 15 becomes

$$I(q) = N(\rho_1 - \rho_2)^2 \left\langle V_1^2 \right\rangle e^{-\langle Rg \rangle_G^2 q^2/3} (q \to 0) \tag{17}$$

where $<V_1^2>$ is the average of V_1^2 and $< R_g >_G$ is a weighted average (named Guinier average) defined as

$$\left\langle R_g \right\rangle_G = \left[\frac{\int N\left(R_g\right) V_1^2 R_g^2 dR_g}{\int N\left(R_g\right) V_1^2 dR_g} \right]^{1/2} \tag{18}$$

with $\int N\left(R_g\right) dR = N$. Notice that the $<\mathrm{R_g}>_\mathrm{G}$ averaging weights more large objects than small ones. For a polydisperse set of spherical nano-objects, Eq. 18 becomes

$$\langle R \rangle_G = \left[\frac{\int N(R) R^8 dR}{\int N(R) R^6 dR} \right]^{1/2} = \left[\frac{\langle R^8 \rangle}{\langle R^6 \rangle} \right]^{1/2} \tag{19}$$

Guinier law is usually applied to determine the radius of gyration of nano-objects with narrow size distribution. For highly polydisperse systems, the q range over

which Guinier law holds is small and Guinier plot yields a weighted average of the radius of gyration far from the arithmetic average and strongly biased toward those of the largest objects. This effect is schematically described for two sets of spherical objects with same arithmetic average radius $<R> = 40$ Å but different widths of radius distribution, as shown in Fig. 3a. For these two systems the slopes of the linear portion of Guinier plots and, consequently, the average radius $<R>_G$ derived by applying Guinier law are different (Fig. 3b). The extrapolated intensity $I(0)$ for polydisperse systems, being proportional to the average $<V_1^2>$, also depends on the shape of the radius distribution.

From Eq. 15, it can be inferred that the experimental SAXS intensity extrapolated to $q = 0$ corresponding to a dilute set of N identical objects is given by $I(0) = N(\Delta n)^2$. For two-electron density systems composed of a dilute set of N nano-objects, each of them with volume V_1 and electron density ρ_1, embedded in a matrix with electron density ρ_2, the SAXS intensity at $q = 0$ is

$$I(0) = N(\rho_1 - \rho_2)^2 V_1^2 \tag{20}$$

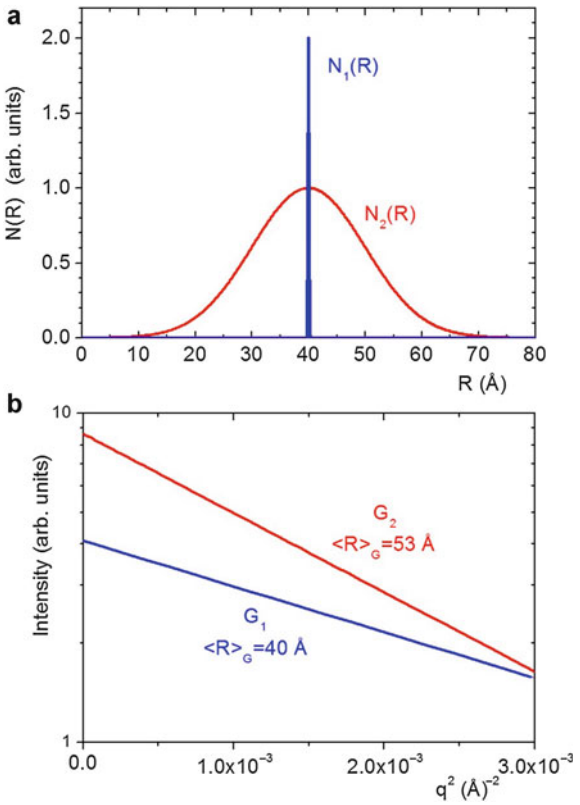

Fig. 3 (**a**) Narrow $N_1(R)$ and wide $N_2(R)$ radius distributions of spheres with same arithmetic radius average $<R> = 40$ Å. (**b**) Guinier plots of SAXS intensities G_1 and G_2, at small q, corresponding to the radius distributions $N_1(R)$ and $N_2(R)$, respectively. The magnitude of the slope of the linear part of the *log I* vs. q^2 plot at small q and the extrapolated intensity $I(0)$ associated to the radius distribution $N_2(R)$ are both higher than for $N_1(R)$

For dilute solutions we have $\varphi_1 V = NV_1$ and $(1-\varphi_1) \approx 1$ so as Eq. 12 becomes $Q = 2\pi^2 N(\rho_1 - \rho_2)^2 V_1$. Thus, regardless the object shape, its volume V_1 can be determined from the quotient $I(0)/Q$ as follows:

$$V_1 = 2\pi^2 \frac{I(0)}{Q} \tag{21}$$

Equation 21 can also be applied to polydisperse systems, the result being in this case the quotient between averages, $<V_1^2>/<V_1>$.

Identical anisotropic objects with same orientation produce anisotropic scattering patterns, i.e., the scattering intensity depends on the direction of the vector $\vec{q}$. In the limit of small $\vec{q}$, Guinier law becomes (Guinier and Fournet 1955)

$$I(q_D) = N(\rho_1 - \rho_2)^2 V_1^2 e^{-R_D^2 q_D^2} \tag{22}$$

where q_D refers to the component of $\vec{q}$ in the direction along which the scattering intensity is measured and R_D is the inertia distance of the object in the same direction, from a perpendicular plane containing the center of "mass" of the electron density function.

If the system is composed of identical and anisotropic nano-objects that are randomly oriented, the resulting scattering intensity is isotropic. In this case, the structural parameter determined by applying Guinier law (Eq. 15) is the radius of gyration of the nano-objects.

Dilute Sets of Nanoparticles

Spherical Nanoparticles

Schematic views of monodisperse and polydisperse sets of spherical nano-objects are shown in Fig. 4a, b, respectively. The scattering intensity associated to a single spherical and homogeneous nano-object embedded in a homogeneous matrix, with spatially constant electron densities ρ_1 and ρ_2, respectively, is derived from the amplitude $A_1(q)$ defined by Eq. 3. For a spherical nano-object with radius R the scattering intensity is given by

$$I_1(q) = |A_1(q)|^2 = \left[(\rho_1 - \rho_2)\int_0^R 4\pi r^2 \frac{\sin qr}{qr} dr\right]^2 \tag{23}$$

By solving the integral, Eq. 23 becomes

$$I_1(q) = \left[(\rho_1 - \rho_2)(4\pi/3)R^3 \Phi(q,R)\right]^2 \tag{24}$$

where $\Phi(q, R)$ is

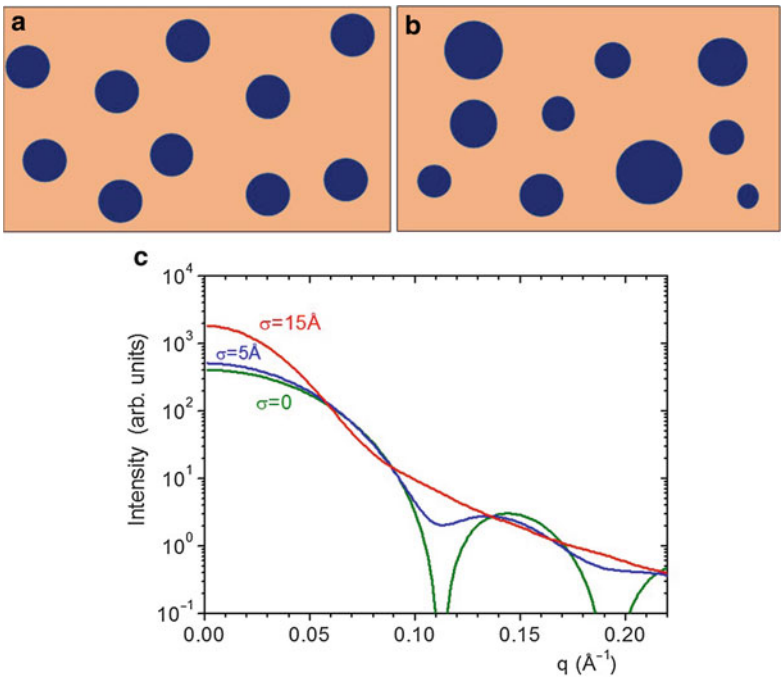

Fig. 4 Schematic views of systems composed of dilute sets of (**a**) monodisperse and (**b**) polydisperse sets of spherical nano-objects. (**c**) Scattering intensities corresponding to three samples containing spherical objects with the same average radius $<R> = 40$ Å and a Gaussian distribution N(R) with three different standard deviations: $\sigma = 0$, $\sigma = 5$ and $\sigma = 15$ Å

$$\Phi(q,R) = 3\frac{\sin qR - qR\cos qR}{(qR)^3}$$

Thus the total scattering intensity produced by a dilute (spatially uncorrelated) set of N identical spheres is $I(q) = NI_1(q)$, i.e.,

$$I(q) = N(\rho_1 - \rho_2)^2\left(\frac{4\pi}{3}R^{3.}\right)^2[\Phi(q,R)]^2 \tag{25}$$

The scattering intensity given by Eq. 25 is plotted in Fig. 4a, for identical spheres with radius $R = 40$ Å. At high q the intensity function exhibits several secondary maxima and zeros, the different zeros being located at $qR = 4.50, 7.72, 10.90 \ldots$

The scattering intensity related to a dilute set of N spherical nano-objects with a radius distribution defined by $N(R)$ is calculated by

$$I(q) = \int N(R)I_1(q,R)dR \tag{26}$$

where $I_1(q, R)$ is the scattering intensity produced by a single sphere (Eq. 24).

The scattering intensity curves related to three dilute sets of spherical objects, with different Gaussian radius distributions and same arithmetic average radius $<R> = 40$ Å, are plotted in Fig. 4c. The standard deviations of the Gaussians are $\sigma = 0$ (monodisperse system), 5 Å and 15 Å. It can be noticed in Fig. 4 that, for increasing polydispersivity, the secondary maxima and zeros progressively smear out. On the other hand, in this case the intensity $I(0)$, being proportional to $<V_1^2>$ or $<R^6>$, is higher for wider radius distributions.

The radius distribution $N(R)$ of a dilute and polydisperse set of spherical nanoparticles can be derived from the measured $I(q)$ functions by solving the integral Eq. 26. For this purpose, the program package named GNOM (Svergun 1992) is often used. The output of GNOM yields the volume weighted distribution function, $D(R)$, related to $N(R)$ for spheres by $D(R) = (4\pi/3)R^3N(R)$. GNOM is also applied to determine the volume distribution function of nano-objects with other simple shapes. Moreover the intensity function $I_1(q)$ related to objects with complex shapes can be independently determined and used as an input file in GNOM program.

Application (Example 1): PbTe Nanocrystals Embedded in a Silicate Glass

An experimental SAXS study of a system composed of PbTe nanocrystals embedded in a silicate glass was performed by Craievich et al. (1997). This nanostructured material exhibits interesting nonlinear optical properties in the infrared, making it potentially useful for applications to telecommunication devices. A silicate glass doped with Pb and Te was held at high temperature, quenched by splat-cooling down to room temperature and then submitted to an isothermal annealing at 650 °C. Initially, isolated Pb and Te atomic species diffuse through the supersaturated glass and nucleate PbTe nanocrystals which progressively grow.

A number of SAXS intensity curves were successively recorded in situ, along the whole annealing process. The experimental results are displayed in Fig. 5. The SAXS intensity progressively increases for increasing annealing time. At high q, the intensity curves exhibit satellite peaks or secondary maxima that are characteristic of the scattering function associated to a set of spheres with nearly identical radius. The secondary maxima progressively shift toward smaller q, as expected for a set of growing nanospheres (Eq. 25). Because of the high statistical dispersion in the scattering intensities at high q, the secondary maxima are not clearly apparent in the curves corresponding to early stages of nanocrystal growth. The positive deviation of the experimental points from the theoretical modeled curve, at very small q, indicates the existence of additional and rather large heterogeneities in electron density in the glass matrix.

The experimental SAXS curves displayed in Fig. 5 were well fitted by model functions defined by Eq. 26, which applies to dilute sets of spherical objects, assuming a time-varying average nanocrystal radius and a Gaussian radius distribution, $N(R)$, with a time-independent relative standard deviation $\sigma/<R> = 0.08$.

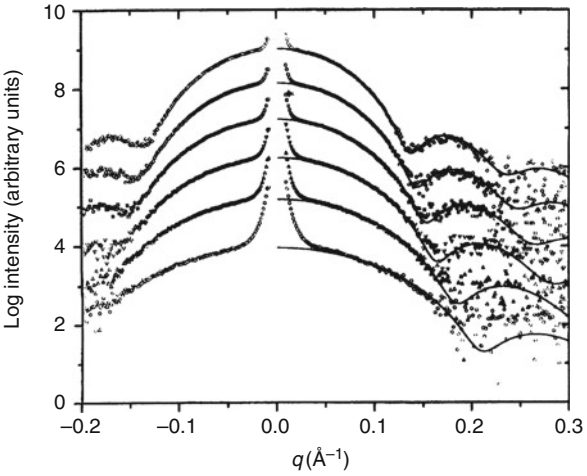

Fig. 5 Scattering intensity curves recorded in situ, corresponding to a dilute set of spherical PbTe nanocrystals embedded in a homogeneous silicate glass, during isothermal growth at $T = 650$ °C. The period of time for nanocrystal growth increases from 19 up to 119 min from bottom to top. The continuous line is the best fits of Eq. 26 using a Gaussian $N(R)$ function with a time-varying radius average and a constant relative standard deviation $\sigma/<R> = 0.08$. The curves are vertically displaced for clarity (Reprinted with permission from Craievich et al. (1997). Copyright 1997 by the International Union of Crystallography)

For the sample held 2 h at 650 °C, the best fit of the model scattering curve led to $<R> = 32.5$ Å and $\sigma = 2.6$ Å. The time dependence of the average radius $<R>$ agrees with the prediction of the classical theory for nucleation and growth of spherical precipitates in a homogeneous matrix.

Application (Example 2): Clustering of Colloidal ZnO Nanoparticles

Powders consisting of ZnO nanoparticles produced by sol-gel route are used as precursors for developments of new materials with interesting properties. The first step of the sol-gel route leading to ZnO solid nanoparticles is the formation of a liquid suspension of zinc acetate in ethanol, to which LiOH is added under ultrasound treatment.

An in situ SAXS study was performed in order to characterize the first steps of aggregation of ZnO nanoparticles in liquid solution (Tokumoto et al. 1999). The different experimental scattering functions, recorded after increasing periods of time at 40 °C, were analyzed by assuming that the system is dilute and that the colloidal nano-objects are spherical. In order to determine the radius distribution of the particles, the integral Eq. 26 was solved by using GNOM program (Svergun and Semenyuk 1991; Svergun 1992). GNOM was applied to all experimental scattering curves of the studied ZnO-based suspension corresponding to different aggregation

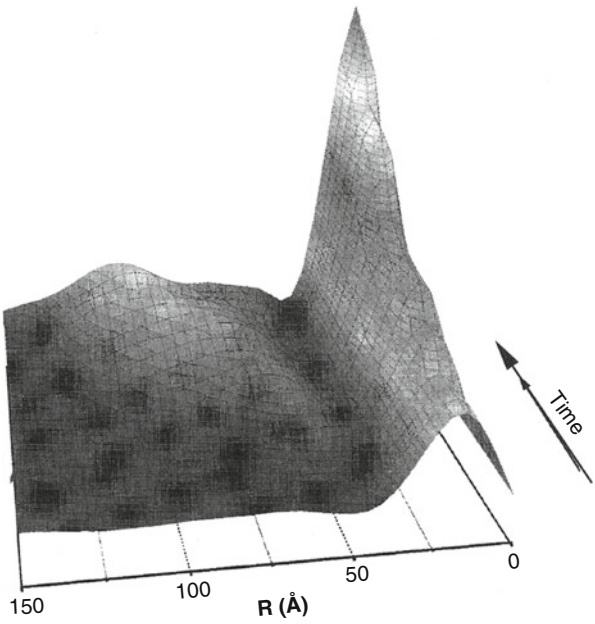

Fig. 6 Time-dependent volume weighted radius distribution, D(R), for ZnO-based colloidal particles in liquid suspension maintained inside a sealed cell during SAXS measurements. The time of growth increases from 10 up to 120 min. The D(R) functions were derived from the set of experimental SAXS curves by applying the GNOM program (Reprinted with permission from Tokumoto et al.(1999). Copyright 1999 by Elsevier)

times, thus yielding the set of volume weighted radius distribution functions $D(R)$ plotted in Fig. 6.

The shape of the $D(R)$ function and its time variation (Fig. 6) suggested that the kinetics of formation of ZnO clusters is characterized by two main stages. During the first stage, a growing peak centered at $R = 17$ Å is apparent, indicating a continuous formation of small clusters. The number of clusters increases monotonously for increasing reaction time, while their average radius, $<R> = 17$ Å, remains constant. During the second stage, the volume weighted distribution exhibits a still growing peak at 17 Å, while the formation and growth of a second peak corresponding to an initial average particle radius $<R> = 60$ Å is also apparent. This peak shifts continuously toward higher R values, up to 110 Å, along a period of time of 2 h. The described time variation of the volume weighted distribution function clearly evidences the continuous formation of colloidal primary clusters and their simultaneous aggregation and growth.

Concentrated Sets of Nanoparticles

Spatially Correlated Spherical Nanoparticles

Many sol-gel based isotropic nanomaterials consist of spatially correlated nanoparticles embedded in a homogeneous matrix. Examples are concentrated colloidal sols (solid nanoclusters embedded in a liquid medium) and solid hybrid

nanomaterials (inorganic clusters embedded in a solid polymeric matrix). Two models of SAXS functions associated to different types of systems composed of spatially correlated nano-objects will be described, one of them containing identical nanoclusters and another consisting of a two-level hierarchical structure.

The total scattering intensity produced by a set of identical and spatially correlated nano-objects is affected by interference effects, thus Eq. 14 does not hold. For isotropic systems composed of a set of N spatially correlated spherical (or more generally centrosymmetrical) nano-objects, the SAXS intensity is given by

$$I(q) = NI_1(q)S(q) \tag{27}$$

where $S(q)$ is the structure function that accounts for interference effects produced by spatial correlation. For a set of nano-objects without long-range order, the structure function $S(q)$ tends asymptotically to 1 at high q. For a set of spatially uncorrelated nano-objects $S(q) = 1$ over the whole q domain, and thus Eq. 27 becomes equivalent to Eq. 14.

A semiempirical structure function that is often applied to describe spatial correlation in isotropic systems composed of spherical nano-objects embedded in a homogeneous matrix, derived using the Born–Green approximation, is given by (Guinier and Fournet 1955):

$$S(q) = \frac{1}{1 + k\Phi_S(q)} \tag{28}$$

where k, named "packing factor," is associated to the degree of compactness of the local structure (for the closest packing of spheres k_{max} is equal to 5.92) and $\Phi_s(q)$ is

$$\Phi_S(q) = 3\frac{\sin qd - qd\cos qd}{(qd)^3} \tag{29}$$

where d is the average distance between the spatially correlated nano-objects.

Several examples of models for scattering intensity functions are displayed in Fig. 7a, b. These functions are determined by Eq. 27 with $S(q)$ given by Eq. 28 for a set of spheres with same radius, $R = 10$ Å, and different d and k values. The intensity curves displayed in Fig. 7a show that the q value corresponding to the maximum of the scattering curves, q_{max}, decreases for increasing average distances. On the other hand, the different curves plotted in Fig. 7b indicate that increasing values of packing factor k yield more pronounced and well-defined scattering peaks. A rough estimate of the average distance between particles is usually inferred by applying the simple equation $d = 2\pi/q_{max}$. However, by analyzing the curves plotted in Fig. 7a, it can be verified that the equation $d = 5.6/q_{max}$ yields a better estimate of the average distance. Anyway, the determination of a more precise average distance between particles requires the fitting of a model intensity function to the whole experimental intensity curve.

Even for nano-objects that are not spherical but instead exhibit a globular shape, the structure function given by Eq. 28 is usually applied as a good approximation.

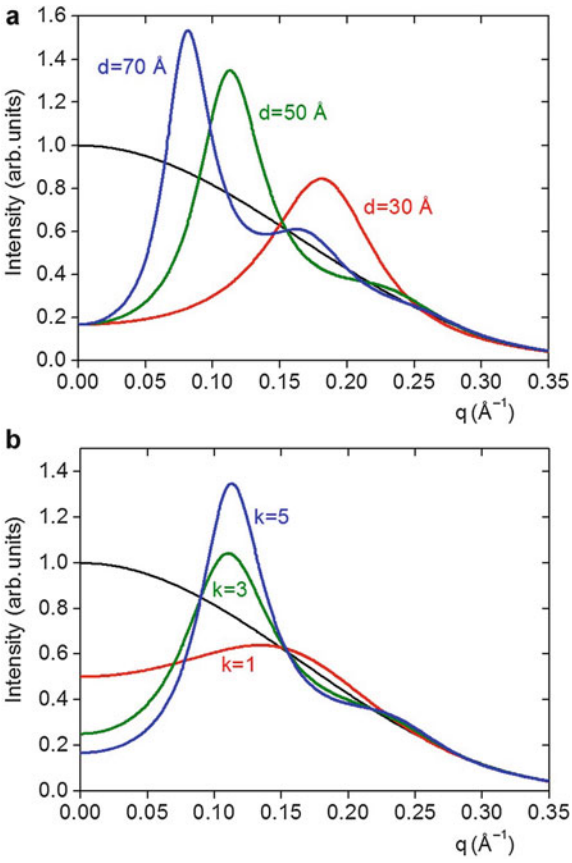

Fig. 7 Model scattering intensity curves corresponding to different sets of spatially correlated spheres, all of them with same radius, $R = 10$ Å. (**a**) Packing factor $k = 3$ and average interparticle distances: $d = 30$ Å, $d = 50$ Å, and $d = 70$ Å. (**b**) Average distance $d = 50$ Å and packing factors $k = 1$, $k = 3$ and $k = 5$. The normalized scattering intensity curve for a *dilute set* of particles with same radius is displayed as a *black line* in (**a**) and (**b**)

This structure function is also applied to model scattering intensity curves associated to materials composed of polydispersed nano-objects with narrow radius distributions.

Many hybrid materials prepared by the sol-gel process were studied by SAXS. Some of these hybrid materials are composed of a isotropic set of inorganic nanoclusters embedded in a polymeric matrix. The heterogeneous nature of these nanostructured materials is characterized by using a simple two-electron density model consisting of high electron density clusters embedded in a low electron density matrix (Dahmouche et al. 1999). Certainly, the polymeric phase exhibits electron density fluctuations at molecular level that also produces small-angle scattering, but their contribution to the total scattering intensity is assumed to be weak and/or not strongly varying with q. The basic assumption here is that the dominant contribution to small-angle scattering intensity comes from the electron density contrast between inorganic nanoclusters and polymeric matrix.

Some materials are heterogeneous at multiple scale levels. For example, nanometric clusters may segregate and form cluster-rich domains embedded in a

cluster-depleted matrix. For this particular two-level system, the effects on the SAXS intensity produced by a coarse structural level and another fine level are expected to be dominant at low and high q, respectively.

For the example to be described in the next section corresponding to a isotropic two-level structure – with its fine level consisting of spatially correlated nano-objects – the scattering intensity can be modeled by the following semiempirical equation (Beaucage et al. 1995):

$$I(q) = \left[G_1 \cdot \mathrm{e}^{-(1/3)R_{g1}^2 q^2} + B_1 \cdot \mathrm{e}^{-(1/3)R_c^2 q^2} \left\{ \left[erf\left(qR_{g1}/6^{1/2}\right)\right]^3 / q \right\}^{P_1}\right] + \left[G_2 \cdot \mathrm{e}^{-(1/3)R_{g2}^2 q^2} + B_2 \cdot \left\{ \left[erf\left(qR_{g2}/6^{1/2}\right)\right]^3 / q \right\}^{P_2}\right] \cdot S(q) \tag{30}$$

where sub-indexes 1 and 2 refer to the coarse and fine structure levels, respectively. The factors G_i are equal to $N_i(\Delta n_i)^2$ (Eq. 15) and B_i are related to G_i by specific equations that depend on the object geometry, and P_i are Porod exponents that are equal to 4 for simple two-electron density systems and may have other values depending on the geometry of the objects. The second term in Eq. 30 corresponding to the fine level also includes the structure function $S(q)$ accounting for spatial correlation of the small clusters inside the volume defining the coarse level. In the first term, associated to the coarse structure, the Gaussian function given by $\exp\left(-R_c^2 q^2/3\right)$ is a high-q cutoff factor in which $R_c = R_{g2}$ (Beaucage et al. 1995).

Provided the X-ray scattering experiment covers a wide q range, hierarchical structures consisting of more than two structure levels can also be characterized. In order to model SAXS intensity curves associated to these complex materials, additional terms are included in Eq. 30. Since the q range to be covered for the study of many-level structures is rather wide, several SAXS measurements with the same sample but using different collimation conditions, sample-to-detector distances and/or X-ray wavelengths, are required. Examples of fittings of model functions assuming multilevel structures to a number of experimental SAXS curves were reported by Beaucage et al. (1995). In order to characterize coarse structures composed of very large (micrometric) particles, the use of ultra-small-angle X-ray scattering (USAXS) – q range below 0.001 Å^{-1} – or light scattering techniques is required.

Application: Fe-Doped Organic–Inorganic Hybrid Nanomaterials

Many organic–inorganic composite materials exhibit interesting properties that can be tailored by an adequate control of the preparation conditions (Dahmouche et al. 1999). Moreover, the structural characterization of these materials is needed in order to explain their magnetic behavior. The structure of a number of hybrids composed of spatially correlated siliceous nanoparticles or clusters embedded in a

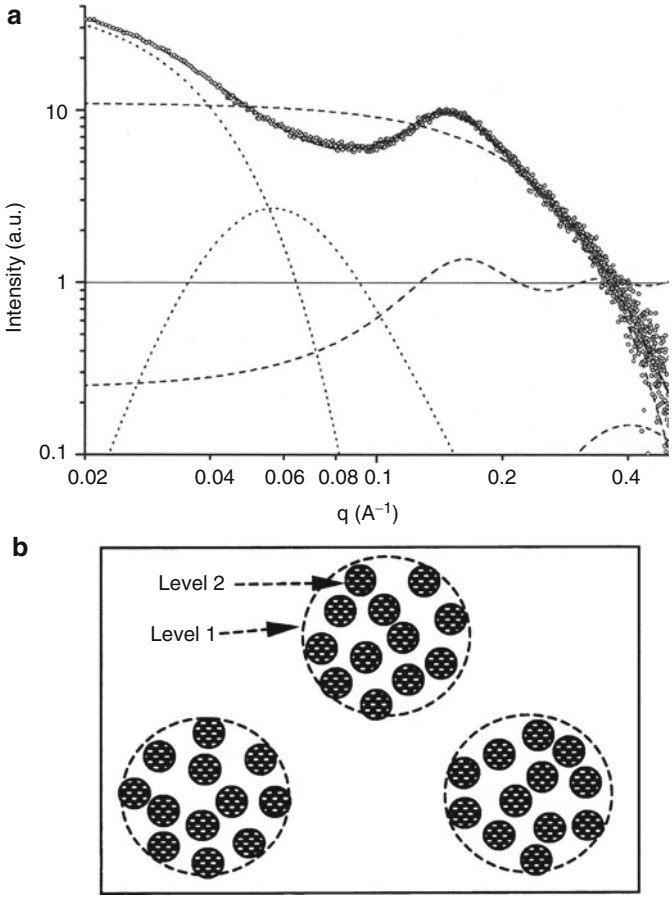

Fig. 8 (**a**) Experimental scattering intensity produced by siliceous clusters containing 0.76 wt% Fe(II) embedded in a polymeric matrix. The continuous line is the best fit of Eq. 30 to the experimental curve. The *dashed lines* indicate the Guinier and Porod contributions to the scattering intensity produced by siliceous clusters and the structure function (oscillatory curve). The *dotted lines* are the Guinier and Porod contributions to the scattering intensity associated to the coarse domains. (**b**) Schematic view of the proposed two-level model. The small circles correspond to siliceous clusters (Figure 8a reprinted with permission from Silva et al. (2003). Copyright 2003 by the International Union of Crystallography)

matrix consisting of grafted polymeric chains were well described by a two-electron density model. For these systems the SAXS patterns exhibit a correlation peak located at decreasing q values for increasing molecular weight of the polymer molecule (Dahmouche et al. 1999).

A SAXS study of hybrid organic–inorganic nanomaterials composed of Fe(II)-doped di-ureasils was carried out by Silva et al. (2003). Figure 8a displays the scattering intensity produced by a di-ureasil hybrid doped with 0.76 wt% Fe(II). In

order to characterize the structure of Fe(II)-doped nanohybrids, the two-level model described in the precedent section (Beaucage et al. 1995) was applied. The SAXS intensity corresponding to the fine structure level displays a peak associated to cluster-cluster correlations, centered at $q = 0.15$ Å^{-1}, which is also observed for undoped samples. For Fe(II)-doped hybrids, this peak is slightly shifted toward higher q. For $q < 0.1$ Å^{-1}, the scattering intensity is mainly related to the coarse structural level. The model scattering curve defined by Eq. 30 for two structural levels, including the structure function $S(q)$ for the fine level given by Eq. 28, is displayed in Fig. 8a. This figure also shows the Guinier and Porod contributions to the total scattering intensity corresponding to both levels. The radii of gyration R_g obtained by the best fit procedure are 7.5 Å for the small clusters and 54 Å for the coarse domains.

Similar analyses of SAXS curves for different Fe(II) doping levels, up to 4.5 wt%, revealed a decreasing average distance between siliceous clusters for increasing Fe(II) content. This result suggests that Fe(II) ions are dispersed in the polymeric matrix, these ions promoting a shrinkage effect that leads to the observed decrease in average cluster-cluster distance.

The model structure consisting of large domains containing spatially correlated siliceous particles embedded in a depleted matrix is schematically shown in Fig. 8b. The reported results indicate that the formation of coarse silicide-rich domains is promoted by the addition of Fe(II) ions (Silva et al. 2003).

Fractal Structures

Small-Angle Scattering by Fractal Structures

The SAXS method is applied to structural characterization of a number of materials which exhibit a self-similar or fractal structure, and also to the determination of the mechanisms involved in aggregation processes, either in precursor sols or after the sol-gel transition.

Fractal materials are characterized by three relevant structural parameters: (i) a radius r_0 corresponding to the size of the individual primary particles (basic nano-objects that build up the fractal structure), (ii) a fractal dimension D that depends on the nature of the mechanism of aggregation, and (iii) a correlation length ξ that defines the size of isolated aggregates or the cutoff distance of the fractal structure for percolated systems such as fractal gels.

A homogeneous object and another with fractal structure – built up by N small primary particles – are schematically shown in Fig. 9a, b, respectively. The number of primary particles inside a sphere of radius r, measured from the center of mass of the fractal aggregate, is given by

$$N(r) = \left(r/r_0\right)^D \tag{31}$$

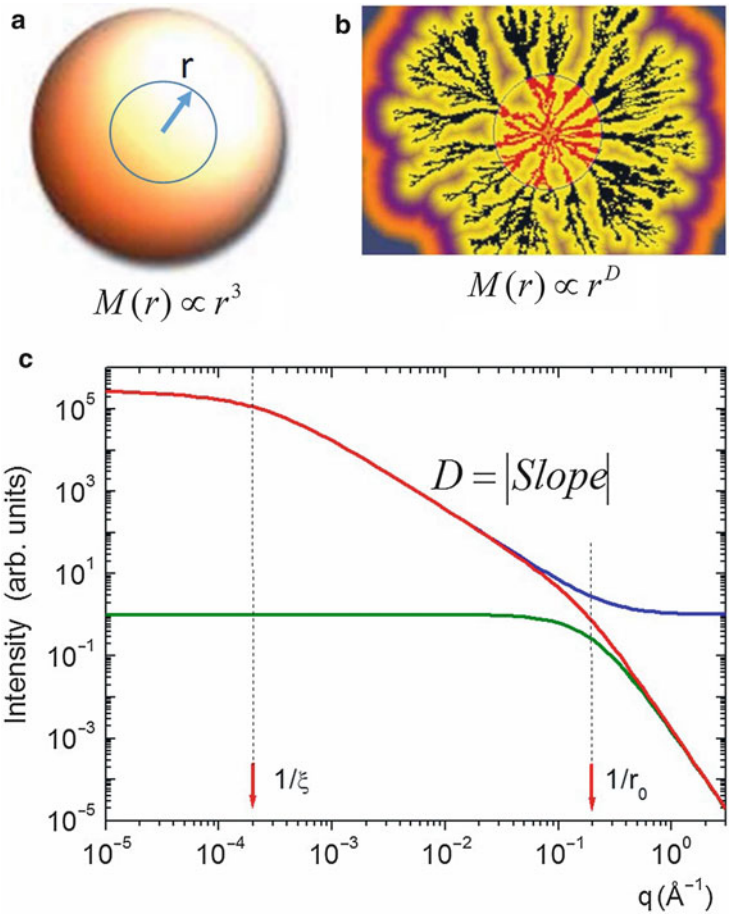

Fig. 9 (**a**) Homogeneous object and (**b**) fractal object. The red curve in (**c**) is the scattering intensity, $I(q) = I_1(q).S(q)$, associated to a fractal object with size of primary building blocks $r_o = 5$ Å, correlation length $\xi = 5000$ Å, and fractal dimension $D = 1.80$. The scattering intensity corresponding to the primary particles, $I_1(q)$ (*olive*), and the structure function, $S(q)$ (*blue*), are also plotted in (**c**). Notice that for large fractal aggregates the determination of the correlation length requires SAXS measurements down to very low minimum q value ($q_{\min} \ll 1/\xi$)

where r_0 is of order of the size of the primary basic units that build up the fractal object. Thus the mass $M(r)$ inside a sphere with radius r, for both (homogeneous and fractal) objects, is proportional to r^D, the exponent being $D = 3$ for homogeneous objects and $D < 3$ for fractal aggregates.

The SAXS intensity associated to a correlated set of primary nanoparticles building up a fractal structure is defined by Eq. 27, which involves the scattering intensity by single primary particles, $I_1(q)$, and the structure function, $S(q)$, associated to the nature of their spatial correlation.

Different simple functions have been used for $I_1(q)$, such as the intensity produced by spherical particles (Eq. 25) or the Debye–Bueche function, defined by

$$I_1(q) = \frac{A}{\left(1 + r_0^2 q^2\right)^2} \tag{32}$$

where A is a constant.

The structure function $S(q)$ corresponding to a fractal object is derived from the radial distribution function for primary particles inferred from Eq. 31. This distribution function is multiplied by a cutting function that defines a structural correlation length ξ. This analysis finally leads to the following structure function (Teixeira 1988):

$$S(q) = 1 + \frac{1}{(qr_0)^D} \frac{D \cdot \Gamma(D-1)}{\left[1 + 1/(q\xi)^2\right]^{(D-1)/2}} \sin\left[(D-1)\tan^{-1}(q\xi)\right] \tag{33}$$

where Γ is the gamma function.

Thus, by selecting $I_1(q)$ defined by Eq. 32 and the structure function $S(q)$ given by Eq. 33, the scattering intensity produced by a fractal aggregate, or by a set of spatially uncorrelated fractal aggregates, is

$$I(q) \propto \frac{1}{\left(1 + r_0^2 q^2\right)^2} \cdot \left\{ 1 + \frac{1}{(qr_0)^D} \frac{D \cdot \Gamma(D-1)}{\left[1 + 1/(q\xi)^2\right]^{(D-1)/2}} \sin\left[(D-1)\tan^{-1}(q\xi)\right] \right\} \tag{34}$$

A scattering intensity function defined by Eq. 34 for particular values of the three structural parameters (r_o, ξ, D) is plotted in log–log scale in Fig. 9c. Since the size of the primary particles is much smaller than the correlation length, $I_1(q)$ is constant within a rather wide low-q range, thus the variation of the scattering intensity at small q's is dominated by the structure function. At high q, $S(q)$ becomes a constant ($S(q) = 1$) and thus the variation in the scattering intensity in this q range is governed by $I_1(q)$.

Figure 9c displays a *log I* vs. *log q* plot associated to a fractal object with correlation length much larger than the size of the primary particles ($\xi \gg r_0$). We notice in this log–log plot the presence of three q ranges over which linear dependences with different slopes are apparent:

(i) Over the small q range ($q \ll 1/\xi$) the slope is zero. In this q range the scattering intensity behaves as expected from Guinier's law, its value extrapolated to $q = 0$, $I(0)$, being related to the fractal dimension D by

$$I(0) \propto \xi^D \qquad \text{or} \qquad I(0) \propto R_g^D \tag{35}$$

with $R_g = \{2/[D(D+1)]\}^{-1/2}\xi$.

(ii) Over the intermediate q range, i.e., for $1/\xi \ll q \ll 1/r_0$, the magnitude of the slope is equal to the fractal dimension D. This implies that the scattering intensity exhibits a simple power q-dependence, $I(q) \propto q^{-D}$.

(iii) Over the high q range ($q \gg 1/r_0$) the slope is -4, this implying that Porod's law ($I(q) \propto q^{-4}$) holds.

Two crossovers of the different linear parts in *log I* vs. *log q* plots, at $q = q_1$ and $q = q_2$ ($q_2 > q_1$), are shown in Fig. 9c. The radius of the primary particles r_0 is simply related to q_2 by $r_0 = 1/q_2$ and the size parameter of the fractal aggregate or correlation length is given by $\xi = 1/q_1$. Thus, if $\xi \gg r_0$, the relevant structure parameters ξ, and r_0 can be directly determined from *log–log* plots of the scattering intensity. If the condition $\xi \gg r_0$ is not satisfied no well-defined crossovers are apparent. In this case, the parameters ξ, D, and r_0, are determined by fitting the $I(q)$ function defined by Eq. 34 to the whole experimental curve.

The fractal dimension D can also be determined by applying Eq. 35 to a set of experimental SAXS curves determined in situ, during an aggregation process. The values of $I(0)$ and R_g are determined from Guinier plots (*Log* $I(q)$ vs. q^2) for all successive SAXS curves. Since $I(0) \propto R_G^D$ the plot of *log* $I(0)$–*log* R_g is expected to be linear, the slope of the straight line yielding the fractal dimension D.

If the condition $\xi \gg r_0$ is not fulfilled the "fractal" model cannot be safely applied. It is a general consensus that, in order to establish the fractal nature of an aggregate, the quotient ξ/r_0 should be of the order of or larger than 10. In addition, it must be remembered that power q-dependences leading to D values smaller than 3 are also expected for nonfractal objects such as, for example, narrow linear chains or thin platelets. Therefore, independent evidences supporting the use of fractal models are often required.

Many mechanisms involved in aggregation processes were analyzed and the respective fractal dimensions of the resulting structures were theoretically determined (Meakin 1986). By associating these theoretical results with experimental determinations of the dimension D, the mechanisms that govern aggregation processes leading to fractal structures can be established.

Applications: Aggregation in Zirconia-Based Sols and Gels

The formation of zirconia-based gels promoted by the aggregation of colloidal particles in sol state was investigated in situ by SAXS (Lecomte et al. 2000). All experimental scattering curves, plotted as *log* $I(q)$ vs. *log q* in Fig. 10, exhibit a wide q range with well-defined linear behavior. Following the procedure described in the precedent section, the magnitude of the slope of the straight line was assigned to the

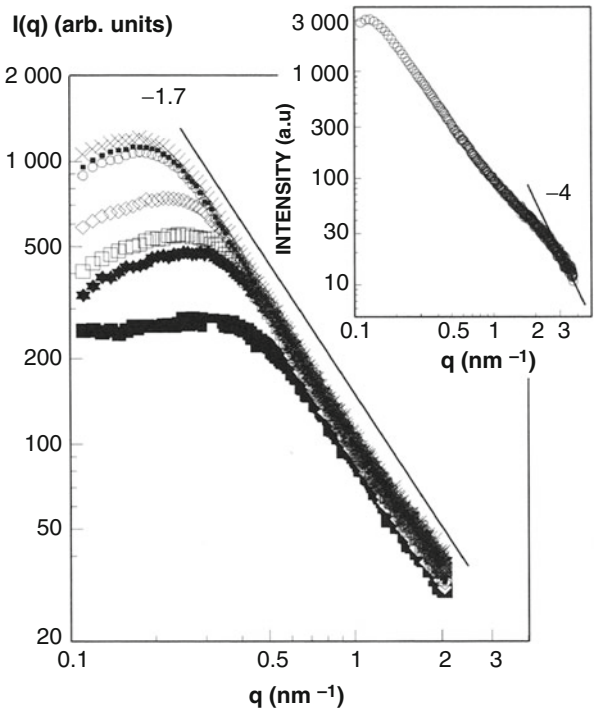

Fig. 10 *Log I* vs. *log q* plots corresponding to a zirconia-based sol held at room temperature for increasing periods of time, from 4 h (*bottom*) up to 742 h (*top*). The inset is the scattering intensity curve of the final gel obtained after a period of about twice the gelling time (Reprinted with permission from Lecomte et al. (2000). Copyright 2000 by the International Union of Crystallography)

fractal dimension of the growing aggregates, D being equal to 1.7 along the whole aggregation process. The low-q limit of the linear portion of the scattering curves displayed in Fig. 10, and thus the crossover q_1, progressively shifts toward lower q for increasing periods of time. This indicates that the aggregate size ($\xi = 1/q_1$) continuously grows. The crossover q_2 is not visible in the main set of curves displayed in Fig. 10 but, in the inset, corresponding to a SAXS curve determined up to a higher q value, this crossover toward a Porod behavior ($I(q) \propto q^{-4}$) is apparent. This suggests that the primary subunits have a smooth and well-defined external surface.

The results reported by Lecomte et al. (2000) indicate that the fractal clusters in the studied zirconia-based sols are formed by aggregation of very small colloidal particles already existing at the beginning of the hydrolysis and condensation reactions. On the other hand, the maximum observed in the scattering curves for $q \neq 0$ is related to the existence of spatial correlations between the fractal aggregates, which could analytically be described by an inter-aggregate structure function $S'(q)$ defined in the same way as $S(q)$, by Eq. 28, and included as another factor in Eq. 34. A fractal dimension close to that experimentally determined ($D = 1.7$) has been derived by computer simulation (Meakin 1986) for the mechanism of growth named diffusion-limited cluster-cluster aggregation (DLCA). Since the slope of all scattering curves displayed in log–log scale does not exhibit any variation with time, it

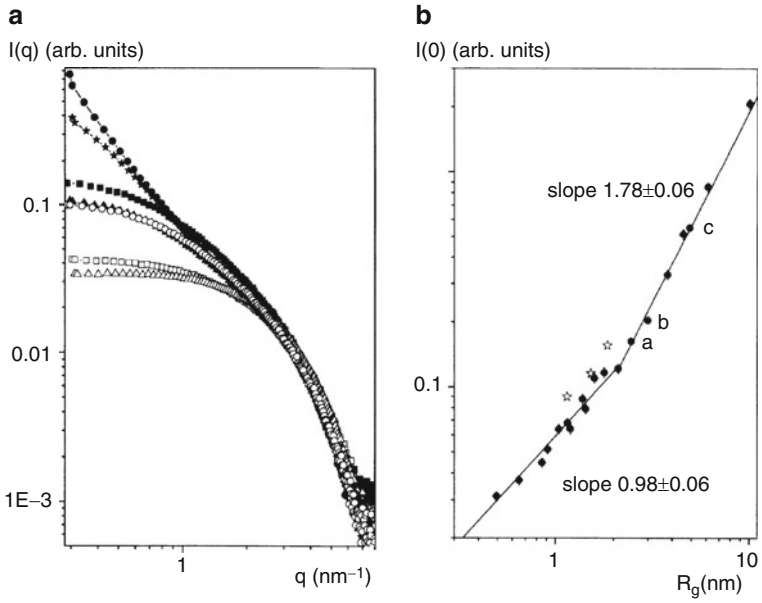

Fig. 11 Scattering intensity curves from sulfate-zirconia sols with different HNO_3, H_2SO_4, and H_2O contents. (**a**) *Log–log* plots of the scattering intensity produced by a few selected samples maintained inside a sealed cell at the end of their aggregation process. (**b**) Plot of $I(0)$ vs. R_g, in *log–log* scale, corresponding to the final states of a number of sols with different compositions (Reprinted with permission from (Riello et al. 2003). Copyright 2003 by the American Chemical Society)

could be concluded that the fractal dimension D and, consequently, the mechanism of aggregation remains invariant during the whole aggregation process.

Another SAXS study of sulfate-zirconia sols with several compositions (varying HNO_3, H_2O and H_2SO_4 contents) was reported by Riello et al. (2003). In order to characterize the aggregation mechanism, these authors determined successive SAXS curves after progressively increasing time periods keeping the sols in open cells. The values $I(0)$ and R_g – determined by applying Guinier law (Eq. 15) to every scattering curve – were plotted as $log\ I(0)$ vs. $log\ R_g$. This plot was analyzed by applying Eq. 35, which predicts for fractal objects a linear behavior with a slope equal to the fractal dimension D of the growing aggregates.

The process of cluster growth in sulfate-zirconia sols with different compositions in sealed cells was also studied. Since, under sealed condition, the reactions in sols are very fast, only the scattering curves corresponding to the final states could be determined (Fig. 11a). The $log\ I(0)$ vs. $log\ R_g$ plot corresponding to the final states of all studied samples is displayed in Fig. 11b. Notice that the experimental points lie on two different straight lines, each of them with a slope similar to those observed by the same authors in previous in situ studies during the cluster growth in open cells.

The slope of the straight line for $R_g < 20$ Å in the $log\ I$ vs. $log\ R_g$ plot displayed in Fig. 11b is close to $D = 1.0$ thus suggesting that the aggregation process starts by the

formation of short 1D linear chains. This initial regime is followed by another one involving the cross-linking of the precursor linear chains which build up a three-dimensional fractal structure. The fractal dimension experimentally determined for $R_g > 20$ Å is 1.8, which is close to the expected theoretical value for diffusion-limited cluster-cluster aggregation. It was then concluded that, even though the sizes of the final aggregates in a number of sols, with very different compositions, vary from 0.5 nm up to 10 nm, the mechanism of growth of all of them is essentially the same.

In the SAXS study reported by Riello et al. (2003) the mechanism of growth of the aggregates is theoretically characterized by an exponent D from the early stages of the clustering process, when the aggregates are still rather small and the condition $\xi \gg r_0$ for a fractal object is not yet fulfilled. Therefore, in these early stages, the exponent D – derived from in situ SAXS experiments by applying Eq. 35 – should not be assigned to a fractal dimension, but instead it must be considered as a useful parameter that characterizes the mechanism of growth.

Nanophase Separation

General Considerations

A number of nanoheterogeneous materials are formed by phase separation processes starting from a homogeneous solid solution at high temperature brought by fast cooling into a miscibility gap. In supersaturated and initially homogeneous (quenched) solid solutions with a composition close to the binodal curve (which defines the solubility limits), phase separation occurs by nucleation and growth of a minor new phase. This leads to a final two-phase material consisting of isolated and initially nanoscopic particles embedded in a homogeneous matrix (Fig. 2a). The growth of the second-phase particles can be characterized by in situ SAXS, using in this case a model consisting of a dilute or concentrated set of spherical particles surrounded by a solute-depleted shell.

On the other hand, the final structure – after long periods of heat treatment – of initially homogeneous solid solutions brought, by quenching, close to the central part of a miscibility gap is described by a two-phase *bicontinuous* model, both phases occupying nearly the same volume fraction (Fig. 2b). For the first stages of phase separation occurring near the central part of the miscibility gap, a theoretical model named spinodal decomposition was proposed by Cahn (1965). At advanced stages of phase separation, even after having reached the equilibrium concentrations, both phases still exhibit a structural evolution driven by a pure coarsening mechanism.

Phase Separation and Dynamical Scaling Property

In order to describe the advanced stages of nanophase separation (i.e., the coarsening regime) in binary materials, a statistical model was proposed by

Marro et al. (1975) and Lebowitz et al. (1982). This model assumes that the material contains atoms A and B arranged in a simple cubic lattice with an occupation function $\eta(r_i)$, which takes values +1 or −1 for sites r_i occupied by atoms A or B, respectively. A probability function for atom exchanges and a simple equation for the energy of the system was proposed. This model is analogous to that applied to ferromagnetic Ising spin systems. Finally, the theoretical isotropic and time-dependent structure function, $S(q, t)$, was determined by computer simulation.

In the proposed model the primary particles are spatially correlated atoms whose scattering intensity $I_1(q)$ at small q is constant. Consequently, the SAXS intensity (Eq. 27) can be written as

$$I(q,t) \propto S(q,t) \tag{36}$$

Different moments $S_n(t)$ and normalized moments $q_n(t)$ of the structure function, $S(q,t)$, are defined as

$$\begin{aligned} S_n(t) &= \int_0^\infty S(q,t) q^n dq \\ q_n(t) &= \frac{\int_0^\infty S(q,t) q^n dq}{\int_0^\infty S(q,t) dq} \end{aligned} \tag{37}$$

Marro et al. (1975) determined the time variation of the structure function $S(q,t)$ and its associated moments at advanced stages of phase separation, after both phases having reached their final compositions. Their results of computer simulations demonstrated that the structure function and its moments exhibit the following properties:

(i) The second moment remains invariant, $S_2(t) = S_2$. Since S_2 is proportional to the integral Q (Eq. 12), its time invariance implies that the advanced stage of phase separation is governed by a pure coarsening process.

(ii) The time variation of the structure function $S(q,t)$ exhibits a dynamical scaling property, evidenced by the existence of a time-independent function $F(x)$ given by

$$F(x) = \frac{S(q,t)}{S_2} [q_1(t)]^{d_s} \tag{38}$$

where the coordinate x is equal to (q/q_1) and d_s is the dimension of the space in which the process of phase separation occurs ($d_s = 3$ for classical 3D processes).

(iii) The normalized first moment of the structure function, $q_1(t)$, exhibits a power time-dependence $q_1(t) \propto t^{-a}$, the parameter a depending on the detailed mechanism of the aggregation of atoms.

(iv) The time dependence of the maximum of the structure function $S(q_m, t)$ is given by $S(q_m, t) \propto t^{a'}$ with $a' = a.d_s$.

All other moments and normalized moments of the structure function are also related by simple mathematical relations. A number of experimental investigations using small-angle (X-ray or neutron) scattering have demonstrated that the described dynamical scaling property also holds for phase separation processes occurring in many nanostructured materials, including glasses (Craievich and Sanchez 1981) and nanoporous xerogels (Santilli et al. 1995).

Since the scattering intensity produced by very small primary particles (atoms) $I_1(q)$ is essentially constant within the small q range, all properties related to the time dependence of the structure function $S(q)$ also apply to the time dependence of the experimental SAXS intensity function $I(q)$.

Application (Example 1): Sintering of SnO_2-Based Xerogels

The theory described in the precedent section referring to phase separation processes in binary materials was applied to understand the structural evolution during isothermal treatment of nanoporous SnO_2 xerogels studied by SAXS (Santilli et al. 1995). These nanoporous materials, after a short transient period, preserve their apparent density thus suggesting that the total fraction of porous volume remains constant during isothermal annealing.

The series of SAXS curves displayed in Fig. 12a, corresponding to a SnO_2-based xerogel isothermally annealed during increasing time periods at 400 °C, exhibit a peak located at progressively decreasing q values. This feature is predicted by the statistical model described in the precedent section. The coincidence of all curves plotted as $[S(q, t)q_1^3/S_2]$ vs. (q/q_1) in Fig. 12b demonstrates that the dynamical scaling property (Eq. 38), theoretically derived for phase separation in simple binary systems, also applies to more complex processes such as the sintering of nanoporous xerogels.

Application (Example 2): Dynamical Scaling of Zirconia-Based Fractal Structures

A demonstration of the dynamical scaling property for a system consisting of fractal zirconia-based aggregates embedded in a liquid matrix was reported by Lecomte et al. (2000). These authors analyzed the set of SAXS curves displayed in Fig. 10, which exhibit a maximum shifting progressively toward lower q for increasing periods of time. As pointed out before, the fractal dimension derived from the linear portions of the *log* $I(q)$ vs. *log* q plots results $D = 1.7$. The same set of curves displayed in Fig. 10 was plotted in Fig. 13 using a $[I(q/q_m) \cdot q^{ds}]$ vs. (q/q_m) scale and setting $d_s = 1.7$. In this analysis, the authors assumed that the first normalized moments q_1 can be replaced as a reasonable approximation by the q-values associated to the maximum of the scattering

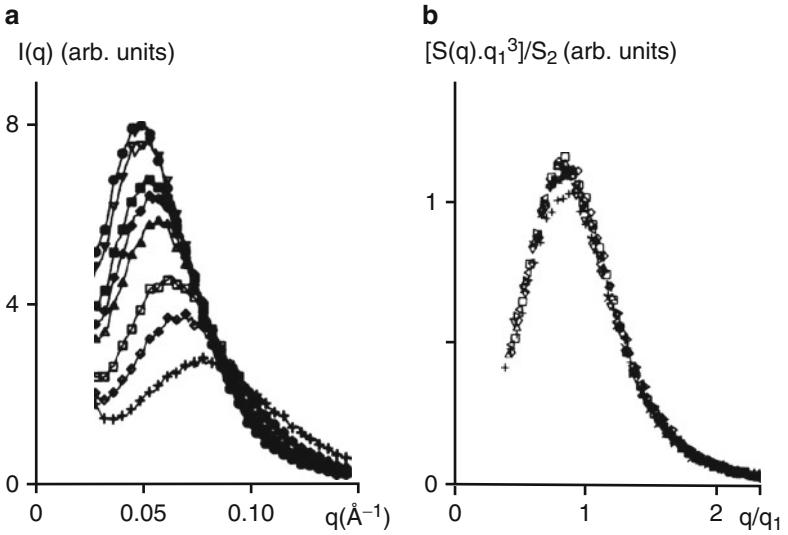

Fig. 12 (**a**) Scattering intensity curves corresponding to a nanoporous SnO_2 based xerogel held at 400 °C after increasing periods of time, from 4.5 min (*bottom*) up to 62 min (*top*). (**b**) Scaled structure functions $[S(q, t)q_1^3/S_2]$ vs. q/q_1 (Reprinted with permission from Santilli et al. (1995). Copyright 1995 by the American Physical Society)

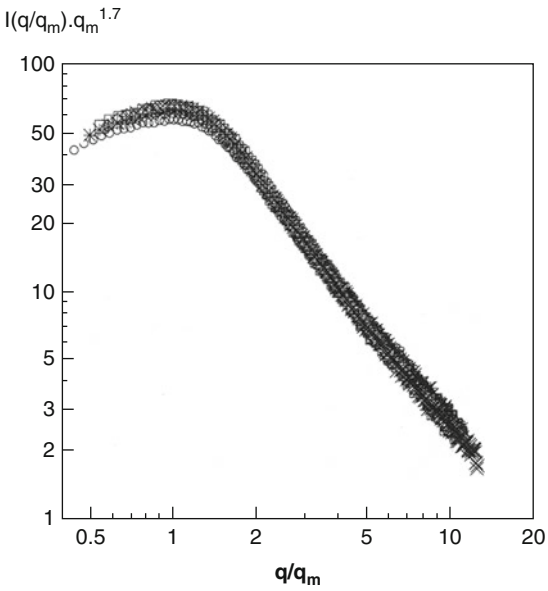

Fig. 13 The same scattering intensity curves displayed in Fig. 10 replotted here as $I(q)q_m^{1.7}$ vs. q/q_m, q_m being the q value corresponding to the maximum of the scattering curves (Reprinted with permission from Lecomte et al. (2000). Copyright 2000 by the International Union of Crystallography)

curves q_m. As it can be seen in Fig. 13 all scattering curves merge into a single scaled curve, this clearly demonstrating that the dynamical scaling property also applies to structural transformations of fractal aggregates.

The results reported by Lecomte et al. (2000) referring to fractal structures demonstrated that the quotient of exponents a' and a associated to the time dependences of the functions $S_m(q_m,t)$ and $q_1(t)$, respectively, would not be equal to the space dimension, $d_s = 3$, but instead equal to the fractal dimension D.

The described experimental results together with those mentioned in the preceding sections and others reported in the literature suggest that the statistical model derived for nanophase separation and particularly the dynamical scaling property of the structure function (Marro et al. (1975)) exhibit universal features, which provide a unified description of processes of structural coarsening in a wide variety of materials.

Grazing Incidence Small-Angle X-Ray Scattering

Basic Concepts

Thin films deposited on solid substrates such as those prepared by spin or dip coating and involving sol-gel transitions deserved the attention of many scientists because of their often interesting technological applications. These films usually have thicknesses ranging from about one nanometer up to a few microns. Since the structure of thin films supported by thick solid substrates cannot be studied by classical transmission SAXS, they are characterized by combining X-ray reflectivity and grazing incidence small-angle X-ray scattering (GISAXS).

X-ray reflectivity measurements allow one to determine the thickness, average mass density, and surface roughness of thin films. Details of this experimental technique are not presented here. Readers interested on the basic concepts and applications of X-ray reflectivity are encouraged to consult the existing bibliography (for example Tolan 1999).

Some thin films are heterogeneous at the nanometric scale. For example, thin films may be composed of a homogeneous matrix containing nanoclusters and/or nanopores, spatially correlated or not. Other materials consist of a homogeneous bulk volume with a thin layer close to their external surface containing buried nanoparticles. These nanoparticles are implanted by sputtering or plasma treatment or formed by nucleation and growth followed by atomic diffusion from supported thin films. GISAXS is usually applied to characterize nanostructured supported thin films and surface layers. Classical GISAXS experiments are performed using a flat sample, the incident beam hitting the sample surface at grazing incidence angles, α_i, typically ~0.3 to 0.6°. The scattering patterns at small angles are recorded by a two-dimensional X-ray detector located at rather long distances from the sample, typically 1–3 m in synchrotron beam lines. Schematic views of the geometry of a GISAXS setup are shown in Fig. 14a, b. Notice that relevant angles in X-ray optics are measured with respect to the sample surface and not with respect to its normal as usual in classical optics.

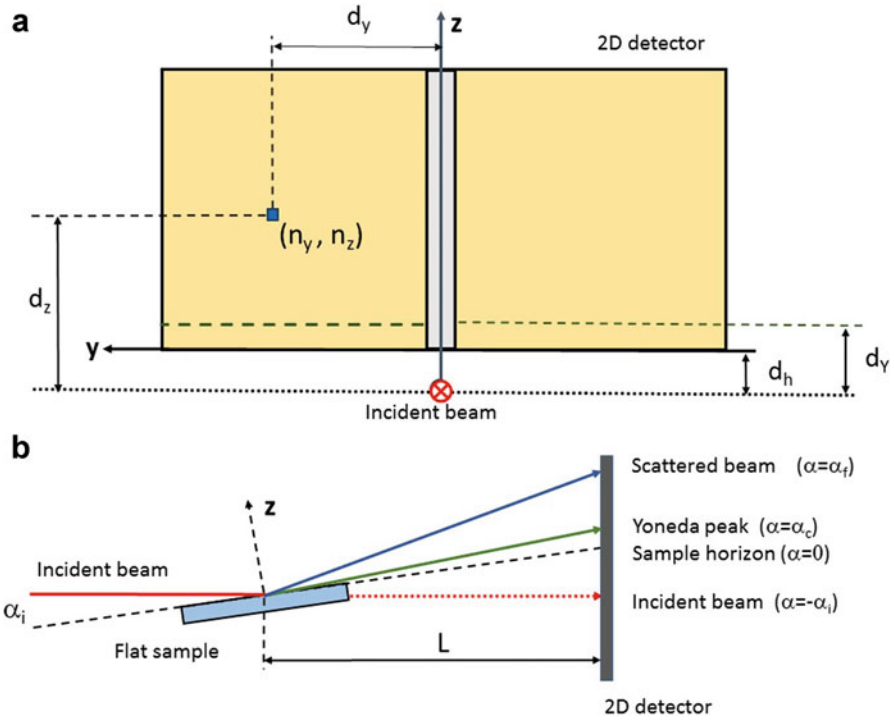

Fig. 14 Schematic GISAXS setup. (**a**) Frontal view of the 2D X-ray detector taken along the direction of the incident beam. The distances that are measured in order to determine the three components of the scattering vector, q_x, q_y, and q_z, associated to each detector pixel (n_y, n_z) (Eq. 39) are indicated. A narrow beam-stopper is usually vertically placed to avoid detector damaging by the strong reflected X-ray beam. (**b**) Lateral view indicating all relevant directions and angles. The GISAXS patterns can be recorded only above the sample horizon (*dashed line*)

The three components of the scattering vector, $\vec{q} = \vec{k} - \vec{k}_0$, associated to a scattered beam hitting a given detector pixel in GISAXS measurements (Fig. 14), are

$$\begin{aligned} q_x &= (2\pi/\lambda)\left(\cos\psi\cos\alpha_f - \cos\alpha_i\right) \\ q_y &= (2\pi/\lambda)\sin\psi\cos\alpha_f \\ q_z &= (2\pi/\lambda)\left(\sin\alpha_f + \sin\alpha_i\right) \end{aligned} \tag{39}$$

The angles α_f and ψ are determined from the vertical (d_z) and horizontal (d_y) distances (Fig. 14) as follows

$$\begin{aligned} \alpha_f &= tg^{-1}[(d_z/L)] - \alpha_i \\ \psi &= tg^{-1}\left(d_y/L\right) \end{aligned} \tag{40}$$

Notice that the detection plane of the 2D detector in real experiments is perpendicular to the incident X-ray beam and not parallel to the normal to sample surface, as

schematically shown in Fig. 14. Anyway, since the incidence angle α_i is very small, the error in the angle α_f associated to the use of this geometry can be neglected.

For a X-ray beam propagating through a medium with refraction index n_0 and hitting a flat interface with another medium with refraction index n, the angle of the refracted beam α_r is determined by applying Snell law, $(n_0/n) = (\cos\alpha_r/\cos\alpha_i)$. For an incident beam in vacuum $(n_o = 1)$ or in a standard gas medium $(n_o \approx 1)$ hitting a flat material surface, the refraction angle results:

$$\alpha_r = \cos^{-1}(\cos\alpha_i/n) \tag{41}$$

For typical (small) incidence angles, α_r is given as a good approximation by

$$\alpha_r = \left(\alpha_i^2 - 2\delta\right)^{1/2} \tag{42}$$

where $\delta = 1 - n$. Since the refraction index of any material for X-rays is slightly lower than $1(\delta \sim 10^{-5})$, there is a critical value of the incidence angle, α_c, for which the refracted beam propagates parallel to the sample flat surface. Substituting $\alpha_r = 0$ in Eq. 42 the critical angle results:

$$\alpha_c = (2\delta)^{1/2} \tag{43}$$

Values of δ for any material composition and X-ray photon energy up to 30 KeV were reported by Henke et al. (1993).

Let us now to describe the main features associated to specular reflection and refraction of an incident monochromatic X-ray beam hitting a flat sample surface under grazing incidence. For different incidence angles the following types of effects occur:

(i) For $\alpha_i < \alpha_c$, the incident beam undergoes specular reflection at an exit angle $\alpha_e = \alpha_i$.
(ii) For $\alpha_i = \alpha_c$, the refracted beam propagates parallel to the sample surface, i.e., $\alpha_r = 0$.
(iii) For $\alpha_i > \alpha_c$, the refracted beam propagates inside the sample in a direction defined by the angle α_r and amplitude $t(\alpha_i)$ given by Snell law and Fresnel transmission function, respectively.

The absorption of X-rays penetrating a flat sample produces a decrease in intensity of the incident beam described by the following basic equation:

$$I(d) = I_0 e^{-(\mu\rho d/\sin\alpha_r)} \tag{44}$$

where I_0 is the intensity of the incident beam, μ is the mass absorption coefficient, ρ is the mass density, and d is the distance from the sample surface.

The *attenuation length* (also named *penetration depth*) is the distance from the surface for which the intensity of the X-ray beam – penetrating into a given material

– becomes equal to I_0/e. This distance is considered to be the approximate thickness of the layer probed in GISAXS measurements. Tables published by Henke et al. (1993) and a program accessible online in their web page yield the attenuation length as a function of the incidence angle, photon energy or wavelength, and sample chemical composition and mass density.

If the incidence angle of the incoming X-ray beam is equal to or lower than the critical angle, an evanescent wave is formed whose penetration depth is only ~5 nm for typical materials. When a thicker layer is desired to be probed using an incident beam with same photon energy, the incidence angle α_i should be set higher than α_c. As an example, Fig. 15a displays the penetration depth of photons in three selected materials, SiO_2, Al, and Ti, for a photon energy $E = 8.04$ KeV (corresponding to $\lambda CuK\alpha = 1.542$ Å) as a function of the incidence angle. Figure 15b shows the same functions for a photon energy $E = 17.44$ KeV ($\lambda MoK\alpha = 0.707$ Å). The curves displayed in Fig. 15a, b indicate that the

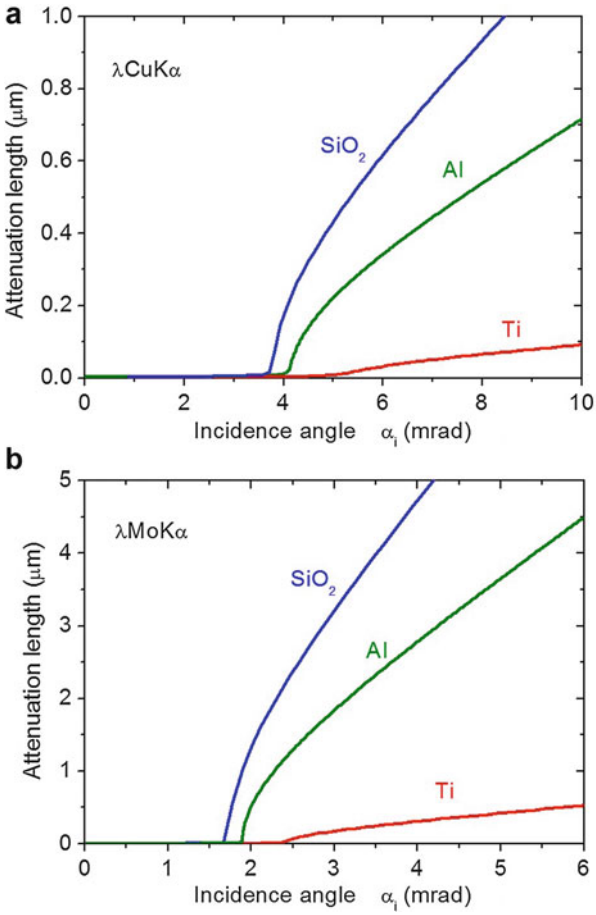

Fig. 15 X-ray attenuation length or penetration depth as function of the incidence angle α_i for three selected materials (SiO_2, Al and Ti) for incident X-ray beams with two different wavelengths: (**a**) Cu λKα (1.542 Å) and (**b**) MoλKα (0.7071 Å). For an incidence angle below the critical angle the attenuation length is very short (a few nanometers)

attenuation length below the critical angle α_c (a few nanometers) is very small for the three selected materials, while for $\alpha > \alpha_c$ the attenuation length exhibits a monotonous increase for increasing incidence angles. Notice that the attenuation length is higher for less dense and lower Z materials. Thus, by adequate choices of incidence angle and photon energy, and depending on material composition and density, a wide range of thicknesses of nanostructured surface layers can be probed.

An additional feature that is apparent in GISAXS patterns is named Yoneda peak (Yoneda 1963), which is associated to interference effects between the reflected and refracted waves. This peak appears at an exit angle $\alpha_Y = \alpha_c$ with respect to the sample surface (Fig. 14a, b).

The analysis of GISAXS results associated to nanostructured thin films and/or to surface layers is performed by fitting model functions to 2D experimental patterns. A reasonable model of a GISAXS function requires an initial guess of particle shape, size distribution, and structure function and should include the Fresnel transmission and reflection functions and the effects associated to Snell law.

More detailed descriptions of GISAXS theory and applications were reported by Kutsch et al. (1997). Moreover, a recent review of modern applications of GISAXS, GISANS (grazing incidence neutron scattering) and grazing incidence X-ray and neutron wide angle scattering was published by Hexemer and Muller-Buschbaum (2015).

Example of Application: Nanostructure of Thin Films Supported by Si Wafers

A simple method for obtaining arrays of $CoSi_2$ nanoplates endotaxially buried in a Si(001) single-crystalline wafer was reported by Kellermann et al. (2012). These authors demonstrated that thermally activated diffusion of Co atoms embedded in a Co-doped SiO_2 thin film deposited on the (001) flat surface of a Si wafer promotes the formation of $CoSi_2$ nanoplates buried inside the Si host. A transmission electron microscopy (TEM) study of this material indicated that the $CoSi_2$ nanoplates exhibit a hexagonal lateral shape, are parallel to Si{111} crystallographic planes, have remarkably uniform sizes, and their lattices are coherently related to the host Si lattice. On the other hand, complementary analyses of TEM images showed the additional presence of a polydisperse set of spherical Co nanoparticles embedded in the supported SiO_2 thin film.

The model GISAXS function for a supported thin film containing an isotropic and dilute set of spherical nanoparticles with a radius distribution $N_{sph}(R)$ is given by

$$I_{sph}\left(q_y,\ q_z\right) \propto |t(\alpha_i)|^2 \left|t\left(\alpha_f\right)\right|^2 \int N_{sph}(R).I_1\left(q_x, q_y, \tilde{q}_z, R\right)dR \qquad (45)$$

where $t(\alpha_i)$ and $t(\alpha_f)$ are Fresnel transmission coefficients (Tolan 1999), $I_1,(q_x, q_y, q_z, R)$ is given by Eq. 24 and refers to the SAXS intensity produced by spherical cobalt nanoparticles with radius R embedded in the silica thin film, and $\tilde{q}_z$ is the z-component of the scattering vector considering that the incident beam scattered by nanoparticles is the refracted beam inside the sample.

On the other hand, the GISAXS function associated to thin hexagonal $CoSi_2$ nanoplates endotaxially buried in Si wafer, with their faces parallel to all Si{111} crystallographic planes, was modeled as (Kellermann et al. 2012; Kellermann et al. 2015):

$$I_{\text{hex}}(q_y, q_z) \propto |t(\alpha_i)|^2 \left|t(\alpha_f\right|^2 (N_{\text{hex}}/4) \sum_{\text{hkl}} \left|A_{\text{hex}}(\text{hkl})(\alpha_i, \varphi, q_x, q_y, \tilde{q}_z, L, T)\right|^2 \quad (46)$$

where N_{hex} is the number of hexagonal nanoplates, A_{hex}(hkl) are the scattering amplitudes associated to regular hexagons oriented parallel to Si{111} crystallographic planes, with thickness T and lateral side L, φ is the azimuthal angle, and $\tilde{q}_z$ is the component of the scattering vector in z direction *inside* the sample.

The total GISAXS function associated to Co nanospheres embedded in the SiO_2 thin film and $CoSi_2$ nanohexagons buried in the Si wafer was modeled assuming independent contributions from both types of nano-objects, i.e.,

$$I_{\text{total}}(q_y, \tilde{q}_z) \propto [I_{\text{sph}}(q_y, \tilde{q}_z) + C.I_{\text{hex}}(q_y, \tilde{q}_z)] \quad (47)$$

where I_{sph} and I_{hex} are given by Eqs. 45 and 46, respectively and C is an adjustable factor.

In modeling the SAXS function, it was assumed that refraction effects are only produced at the interface between air and the SiO_2 thin film. Because of the relatively low difference in density between the SiO_2 thin film containing Co nanoparticles and the Si substrate, refraction effects associated to this interface were neglected.

Kellermann et al. (2015) studied Co-doped SiO_2 thin films deposited on silicon wafers with different surface orientations, namely, Si(001), Si(011), and Si(111), all of them previously heat treated at 750 °C under identical conditions. Experimental 2D GISAXS patterns corresponding to different wafer orientations and the associated theoretical curves modeled by applying Eq. 47 are displayed in Fig. 16.

The analysis of the experimental GISAXS results demonstrated that the sizes of the $CoSi_2$ nanohexagons are functions of the crystallographic orientation of the Si substrate, the lateral size of the nanohexagons buried in Si(111) wafers being remarkably (~50%) larger than those grown inside the other two substrates, Si(011) and Si(001). The thickness of the platelets also varies for different Si substrate orientations from 2.8 nm for Si(001) up to 5.7 nm for Si(111). On the other hand, the spherical Co nanoparticles embedded in the SiO_2 thin film exhibit average radii ranging from 0.6 nm for Si(011) up to 1.5 nm for Si(001).

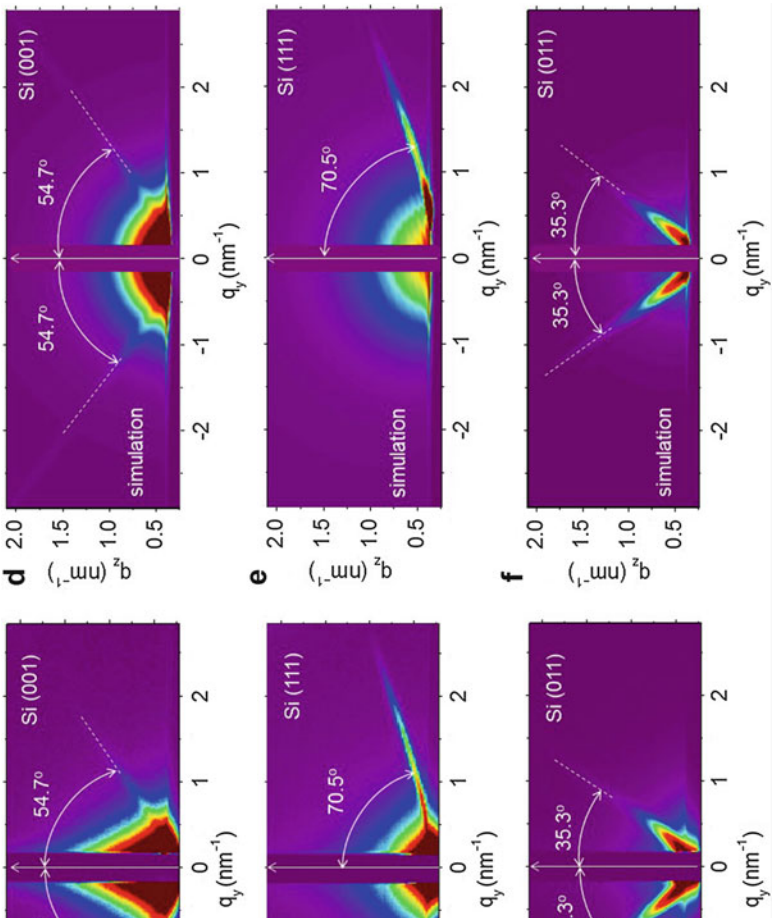

Fig. 16 Experimental 2D GISAXS patterns corresponding to Co-doped SiO_2 thin films deposited on (**a**) Si(001), (**b**) Si(111), (**c**) Si(011) flat wafers. Pictures (**d**–**f**) are the calculated patterns (Eq. 47) that best fit the patterns (**a**–**c**), respectively. The main axes of all elongated lobes in GISAXS patterns are perpendicular to Si{111} crystallographic planes (Reprinted from Kellermann et al., Phys. Chem. Chem. Phys. 2015; 17: 4945–4951)

In conclusion, the GISAXS study reported by Kellermann et al. (2015) led to a complete low-resolution characterization of the nanostructures developed in -Co-doped SiO_2 thin films deposited on Si(001), Si(011), and Si(111) substrates.

Final Remarks

A relevant issue omitted in this chapter is the experimental method that uses the properties of "anomalous" (or resonant) small-angle X-ray scattering (ASAXS), which is today widely applied thanks to the availability of tunable synchrotron X-ray sources (Goerigk et al. 2003). ASAXS is particularly useful for structural studies of biphasic materials with low contrast in electron density and also for analyses of complex multiphase systems.

Additional information about SAXS theory is presented in the classical book authored by Guinier and Fournet (1955) and the book edited by Glatter and Kratky (1982). Another book dealing with SAXS, SANS, and light scattering was edited by Lindner and Zemb (1991). Instrumentation issues mainly focusing on SAXS using synchrotron radiation were described by Russell (1991), and SAXS/SANS studies of the structure and structural changes of biological macromolecules in solution were reviewed by Koch et al. (2003). A useful booklet for beginners was written by Schnablegger and Singh (2013).

Besides the already mentioned GNOM software for SAXS data analysis (Svergun and Semenyuk 1991), new packages such as the recently developed SASFit (Kohlbrecher and Bressler 2014) are available to interested users.

The amount of published articles based on the use of SAXS and SANS exhibited a fast increase during the past three decades (Craievich and Fischer 2010). This fast growth was primarily due to the increasing interest of scientists for studies of structural and physicochemical properties of nanomaterials. Other reasons that explain the observed strong growth in the annual number of published articles are: (i) the commercial availability of modern SAXS setups equipped with novel X-ray sources, focusing and collimating optics and fast high-resolution 2D detectors, (ii) the development of new theoretical approaches and numerical methods for data analysis, (iii) the increasing availability of powerful computers, and (iv) the opening of new small-angle scattering beam lines in many synchrotron and neutron laboratories around the world.

Appendix: Experimental Issues

Basic Comments

Monochromatic X-ray beams are characterized by their photon energy E or wavelength λ, both related by $\lambda = hc/E$, where h is the Plank constant and c is the speed of light in vacuum, i.e., $\lambda(\text{Å}) = 12.398/\text{E(KeV)}$. The wavelengths of typical monochromatic beams

used in SAXS experiments are within the range 0.6–2.0 Å circa (i.e., photon energies ranging from ~6 to ~20 KeV). The X-ray beams produced by synchrotrons or typical commercial sources are usually monochromatized by quartz, germanium, or silicon single crystals, which yield incident beams with very narrow pass-bands ($\Delta\lambda/\lambda < 10^{-3}$).

Considering, for example, a typical SAXS experiment with an X-ray wavelength $\lambda = 1.542$ Å (λCuKα), a sample-to-detector distance $D = 1$ m, a beam-stopper with a diameter $\phi_1 = 5$ mm and a circular 2D detector with a diameter $\phi_2 = 150$ mm, and remembering that $q = (4\pi/\lambda)\sin\theta \approx (2\pi/\lambda).2\theta$ for low q, the range of scattering angles to be covered results $0.14^\circ < 2\theta < 4.3^\circ$, and the corresponding minimum and maximum q values are 0.01 $Å^{-1}$ and 0.30 $Å^{-1}$, respectively. Different lower and upper q limits can be reached by selecting adequate beam collimation, sample-to-detector distances and/or X-ray wavelengths. The choice of the experimental q range depends on the sizes of the nanoparticles to be studied.

X-ray beams for SAXS experiments are produced by classical sealed X-ray tubes, rotating anode X-ray generators and synchrotron sources. Synchrotron radiation sources are often preferred because they provide powerful, continuously tunable and well collimated X-ray beams. Another closely related experimental technique often used for same or similar purposes is small-angle neutron scattering (SANS), its basic theory being essentially the same as that developed for the SAXS technique.

Choice of Sample Thickness

Classical SAXS experiments are performed in transmission mode and usually under normal incidence. The first step for planning SAXS experiments is to determine the sample thickness that maximizes the scattering intensity for a given material and photon energy. The SAXS intensity produced by any material with arbitrary structure, as a function of sample thickness t, is given by

$$I(t) \propto te^{-\mu\rho t} \tag{48}$$

where ρ is the mass density and μ the mass X-ray absorption coefficient, which is a function of chemical composition of the material and photon energy. The absorption coefficient can be obtained from tables published by Henke et al. (1993) or by using an online program accessible in their web page.

Examples of the function defined by Eq. 48 are plotted in Fig. 17 for three different materials. The optimum thickness t_{max} corresponding to the maximum of the $I(t)$ function is

$$t_{\max} = (\rho\mu)^{-1} \tag{49}$$

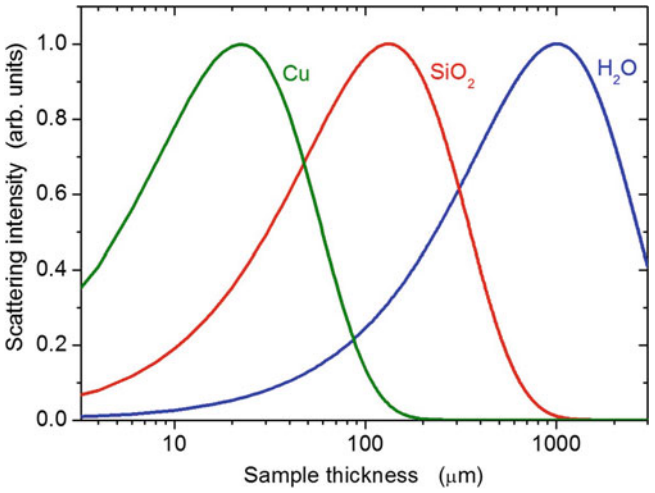

Fig. 17 (**a**) Examples of scattering intensities in arbitrary units as functions of sample thickness for an incident X-ray beam with a wavelength $\lambda CuK\alpha = 1.542$ Å, corresponding to different selected materials: Cu, SiO_2, and H_2O, whose optimum thicknesses t_{max} are 22 μm, 132 μm, and 1.00 mm, respectively

This implies that the transmittance of samples with optimum thickness is

$$T = (I_{\text{transmitted}}/I_{\text{incident}}) = e^{-1} = 0.37. \tag{50}$$

Notice that the t_{max} values determined by Eq. 49 are just a guide for a convenient choice of sample thickness. However, it is always advisable to avoid the use of very thick or very thin samples which would lead to high absorption and low probed volumes, respectively, both yielding weak scattering intensities.

For samples containing large fractions of high Z atoms the optimum thicknesses could be extremely low using CuλKα photons ($E = 8.04$ KeV). For these materials X-ray beams with higher photon energy should be employed. On the other hand, in order to minimize fluorescence effects, the use of beams with photon energies above and close to absorption edges of sample elements should be avoided.

Subtraction of Parasitic Scattering

Before further analysis of experimental SAXS results, a pretreatment of rough data is required. For anisotropic 2D SAXS patterns, the vector $\vec{q}$ associated to each detector pixel is calculated. For isotropic 2D SAXS patterns, the scattering intensity is defined as a function of the modulus of the scattering vector, which is determined by circular averaging.

In order to subtract the parasitic scattering intensity produced by slits, cell windows, and air, two SAXS patterns should be recorded: (i) the total scattering intensity (from sample plus parasitic scattering) defined by the counting rate $R_T\left(\vec{q}\right)$ and (ii) the parasitic scattering intensity given by the counting rate $R_P\left(\vec{q}\right)$ recorded under same experimental conditions but without sample. The scattering intensity exclusively related to the sample is given by

$$R\left(\vec{q}\right) = \left[\left(R_T\left(\vec{q}\right) - R_D\right)/T_{S+W}\right] - \left[\left(R_P\left(\vec{q}\right) - R_D\right)/T_W\right] \tag{51}$$

where R_D is the counting rate associated to the detector noise, T_{S+W} is the transmittance of the sample and cell thin windows, and T_W is the transmittance of the empty sample cell. For solid samples placed in a windowless holder, we have $T_W = 1$. Often the counting rate associated to parasitic scattering for macromolecules in dilute solution is determined with the sample cell filled with same buffer, thus under this condition the scattering intensity due to statistical density fluctuations in the solvent is also subtracted.

When SAXS experiments are conducted using synchrotron beam lines with continuously decreasing electronic current, the effects of time variation of the intensity of the incident X-ray beam should be properly accounted for.

Correction of Smearing Effects

The use of X-ray incident beam with rather large cross-section and/or X-ray detectors with large pixel size may produce serious smearing effects on the SAXS curves. However, most of the modern commercial setups and synchrotron beam lines provide an incident beam with pinhole-like cross-section and use X-ray detectors with very small pixel size, thus often making mathematical desmearing procedures unnecessary.

When using commercial setups yielding an incident X-ray beam with large cross section (for example a beam with linear cross-section), two approaches can be applied for quantitative analyses: (i) fitting the theoretical model of SAXS curve to previously *dismeared* experimental functions or (ii) fitting the previously *smeared* theoretical model of SAXS curve to the experimental function. Since mathematical desmearing of experimental SAXS patterns leads to results with rather high statistical noise, the second procedure is generally preferred.

Determinations of SAXS Intensity in Relative and Absolute Units

For pin-hole collimation of the incident beam, the counting rate $R\left(\vec{q}\right)$ corresponding to the X-ray photons scattered by the sample is proportional to the

$I\left(\vec{q}\right)$ function used along this chapter. Thus Eq. 51 directly yields the scattering intensity in relative scale or arbitrary units, to which model functions are fitted after adequate scaling. However, the SAXS intensity given in absolute scale provides additional information that is often useful for detailed structural characterization.

The typical scattering intensity function in absolute scale is the differential scattering cross-section per unit volume ($d\Sigma/d\Omega$). This function is related to the SAXS intensity $I\left(\vec{q}\right)$, which was used along this chapter, by $(d\Sigma/d\Omega)\left(\vec{q}\right) = I\left(\vec{q}\right).r_e^2/V$.

For SAXS measurements using pin-hole collimation (i.e., with a point-like incident beam cross-section), the differential scattering cross-section per unit volume is given by

$$\frac{d\Sigma}{d\Omega}\left(\vec{q}\right) = \frac{R\left(\vec{q}\right)/\eta}{I_0 V.\Delta\Omega} \tag{52}$$

where $R\left(\vec{q}\right)$ is the photon counting rate, η is the detector efficiency, I_0 is the photon flux of the incident X-ray beam (number of photons per unit cross-section.second), V is the probed sample volume, and ΔΩ is the solid angle associated to the surface area of the detector pixel. The usual unit for the differential scattering cross-section per unit volume is cm^{-1}. Equation 52 can also be written as

$$\frac{d\Sigma}{d\Omega}\left(\vec{q}\right) = \frac{R\left(\vec{q}\right).L^2}{R_0 t_s \Delta a} \tag{53}$$

where R_0 is the counting rate (number of photons/second) corresponding to the total incident beam, t_s is the sample thickness, Δa is the surface area of the detector pixel, and L is the sample-to-detector distance. It is assumed in Eq. 53 that the efficiency of the detectors that records $R\left(\vec{q}\right)$ and R_o are identical. When different detectors are used for the measurements $R\left(\vec{q}\right)$ and R_o, the counting rates should be properly normalized to equivalent efficiencies.

Equation 53 is usually applied to plate-shaped solid samples or to liquids contained in cells with parallel thin windows for entrance of the incident X-ray beam and exit of the scattered photons. Determinations of SAXS intensity in absolute units associated to powdered samples or liquid samples contained in cylindrical capillaries are also possible but their evaluation is less precise (Fan et al. 2010).

Since the measurement of R_o is in practice difficult using standard detectors, the differential scattering cross-section per unit volume of solid materials is generally

determined by means of an independently calibrated sample, such as Lupolen or glassy carbon (Fan et al. 2010).

In order to determine the differential scattering cross-section per unit volume associated to colloidal particles embedded in a liquid medium, it is also recorded – under the same experimental conditions – the SAXS intensity produced by statistical density fluctuations in water. The differential scattering cross-section per unit volume of water $(d\Sigma/d\Omega)_{H_2O}$ – which is a isotropic and constant function at small q – is given by (Guinier and Fournet 1955):

$$\left(\frac{d\Sigma}{d\Omega}\right)_{H_2O}(q \to 0) = (N_{H_2O} n_e r_e)^2 kT\beta \tag{54}$$

where N_{H_2O} is the number of water molecules per unit volume, n_e is the number of electrons per water molecule, k is the Boltzmann constant, T is the absolute temperature, and β is the isothermal compressibility of water at room temperature. Since all parameters in Eq. 54 are known, the differential scattering cross-section per unit volume of water can be written as

$$\left(\frac{d\Sigma}{d\Omega}\right)_{H_2O}(q \to 0) = 1.65.10^{-2}\text{cm}^{-1} \tag{55}$$

If the counting rate associated to a isotropic liquid sample (for example proteins in liquid buffer), $[R(q)]_{\text{sample}}$, and that corresponding to water, $R(q)_{H_2O}$, are determined under same experimental conditions, the differential scattering cross section per unit volume of the studied sample is given by

$$\frac{d\Sigma}{d\Omega}(q) = 1.65.10^{-2}\frac{[R(q)]_{\text{sample}}}{< R(q)_{H_2O} >}\text{cm}^{-1} \tag{56}$$

where $< R(q)_{H_2O} >$ is an average value taken within the small q range over which the counting rate is approximately constant. If SAXS measurements corresponding to sample and water are conducted under different experimental conditions, adequate corrections should be applied. Additional details on this matter were reported by Fan et al. (2010).

Acknowledgments The author thanks the staff of the National Synchrotron Radiation Laboratory (LNLS), Campinas, Brazil, where the experimental parts of most of the SAXS investigations reported in this chapter were conducted; G. Kellermann and C. Huck-Iriart for their useful remarks; and H. Fischer for his help for figures preparation.

References

Beaucage G, Ulibarri T, Black EP, Shaeffer DW. Chapter 9. Multiple size scale structures in silica-siloxane composites studied by small-angle scattering. In: Mark JE, Lee CYC, Bianconi PA, editors. Hybrids organic–inorganic composites, vol. ACS series 585. Washington, DC: American Chemical Society; 1995. p. 97–111.

Cahn JW. Phase separation by spinodal decomposition in isotropic systems. J Chem Phys. 1965;42:93.
Ciccariello S. The leading asymptotic term of the small-angle intensities scattered by some idealized systems. J Appl Crystallogr. 1991;24:509–15.
Ciccariello S, Schneider JM, Schonfeld B, Kostorz G. Illustration of the anisotropic Porod law. J Appl Crystallogr. 2002;35:304–13.
Craievich AF, Alves OL, Barbosa LC. Formation and growth of semiconductor PbTe nanocrystals in a borosilicate glass matrix. J Appl Crystallogr. 1997;30:623–7.
Craievich AF, Fischer H. Quantitative analysis and relevant features of the scientific literature related to SAXS and SANS. J Phys Conf Ser. 2010;247:012003.
Craievich AF, Sanchez JM. Dynamical scaling in the glass system B_2O_3–PbO–Al_2O_3. Phys Rev Lett. 1981;47:1301311.
Dahmouche K, Santilli CV, Pulcinelli SH, Craievich AF. Small-angle X-ray scattering study of sol–gel-derived siloxane-PEG and siloxane-PPG hybrid materials. J Phys Chem B. 1999;103:4937–42.
Debye P, Bueche AM. Scattering by an inhomogeneous solid. J Appl Phys. 1949;20:51525.
Fan L, Degen M, Bendle S, Grupido N, Ilavsky J. The absolute calibration of a small-angle scattering instrument with a laboratory X-ray source. J Phys Conf Ser. 2010;247:012005.
Glatter O, Kratky O, editors. Small-angle X-ray scattering. London: Academic; 1982.
Goerigk G, Haubold HG, Lyon O, Simon JP. Anomalous small-angle X-ray scattering in materials science. J Appl Crystallogr. 2003;36:425.
Guinier A, Fournet G. Small-angle scattering of X-rays. New York: Wiley; 1955.
Henke BL, Gullikson EM, Davis JC. X-ray interactions: photoabsorption, scattering, transmission and reflection at E = 50-30000 eV and Z = 1-92. Atomic Data and Nuclear Data Tables. 1993;54:181–342. http://henke.lbl.gov/optical_constants/
Hexemer A, Muller-Buschbaum P. Advanced grazing incidence techniques for modern soft-matter materials analysis. IUCrJ. 2015;2:106–25.
Kellermann G, Montoro LA, Giovanetti LJ, Santos Claro PC, Zhang L, Ramirez AJ, Requejo FG, Craievich AF. Formation of an extended $CoSi_2$ thin nanohexagons array coherently buried in silicon single crystal. Appl Phys Lett. 2012;100:063116.
Kellermann G, Montoro LA, Giovanetti LJ, dos Santos Claro PC, Zhang L, Ramirez AJ, Requejo FG, Craievich AF. Controlled growth of extended arrays of $CoSi_2$ hexagonal nanoplatelets buried in buried in Si(001), Si(011) and Si(111) wafers. Phys Chem Chem Phys. 2015;17:4945–51.
Koch MHJ, Vachette P, Svergun DI. Small-angle scattering: a view on the properties, structures and structural changes of biological macromolecules in solution. Q Rev Biophys. 2003;36:147–227.
Kohlbrecher J, Bressler I. Software package SASfit for fitting small-angle scattering curves. 2014. http://kurweb.psi.ch/sans1/SANSSoft/sasfit.html
Kustch B, Lyon O, Schmitt M, Mennig M, Schmidt H. Small-angle X-ray scattering experiments in grazing incidence on sol–gel coatings containing nano-scaled gold colloids: A new technique for investigating thin coatings and films. J Appl Crystallogr. 1997;30:94956.
Lebowitz JL, Marro J, Kalos MK. Dynamical scaling of structure-function in quenched binary-alloys. Acta Metall. 1982;30:297–310.
Lecomte A, Dauger A, Lenormand P. Dynamical scaling property of colloidal aggregation in a zirconia-based precursor sol during gelation. J Appl Crystallogr. 2000;33:496–9.
Lindner P, Zemb T, editors. Neutron, X-ray and light scattering. Amsterdam: North Holland; 1991.
Marro J, Boltz AB, Kalos MH, Lebowitz JL. Time evolution of a quenched binary alloy. II. Computer simulation of a three-dimensional model system. Phys Rev B. 1975;12:2000–11.
Meakin P. In: Stanley HE, Ostrowsky N, editors. On growth and form. Boston: Martinus Nijhoff; 1986. p. 111–35.
Porod G. Chapter 2: General theory. In: Glatter O, Kratky O, editors. Small-angle X-ray scattering. London: Academic; 1982.
Riello P, Minesso A, Craievich AF, Benedetti A. Synchrotron SAXS study of the mechanisms of aggregation of sulfate zirconia sols. J Phys Chem B. 2003;107:3390–9.

Ruland W. Small-angle scattering of 2-phase systems. Determination and significance of systematic deviations from Porod's law. J Appl Crystallogr. 1971;4:70.
Russell TP. Chapter 11: Small-angle scattering in synchrotron radiation sources. In: Brown GS, Moncton DE, editors. Handbook on synchrotron radiation, vol. 3. Amsterdam: North Holland; 1991.
Santilli CV, Pulcinelli SH, Craievich AF. Porosity evolution in SnO_2 xerogels during sintering under isothermal conditions. Phys Rev B. 1995;51:8801–9.
Schnablegger H, Singh Y. The SAXS guide. Graz: Anton Paar GmbH; 2013.
Shull CG, Roess LC. X-ray scattering at small angles by finely-divided solids. I. General approximate theory and applications. J Appl Phys. 1947;18:295–307.
Silva NJO, Dahmouche K, Santilli CV, Amaral VS, Carlos LD, V. BZ, Craievich AF. Structure of magnetic poly(oxyethylene)-siloxane nanohybrids doped with Fe-II and Fe-III. J Appl Crystallogr. 2003;36:961–6.
Svergun DI. Determination of the regularization parameter in indirect-transform methods using perceptual criteria. J Appl Crystallogr. 1992;25:495–503.
Svergun DI. Restoring low resolution structure of biological macromolecules from solution scattering using simulated annealing. Biophys J. 1999;77:2879–86.
Svergun DI, Semenyuk A. Small-angle scattering data processing using the regularization technique.1991. www.embl-hamburg.de/biosaxs/gnom.html
Teixeira J. Small-angle scattering by fractal systems. J Appl Crystallogr. 1988;21:781–5.
Tokumoto MS, Pulcinelli SH, Santilli CV, Craievich AF. SAXS study of the kinetics of formation of ZnO colloidal suspensions. J Non-Cryst Solids. 1999;247:176–82.
Tolan M. X-ray scattering from soft-matter thin films. Berlin: Springer; 1999.
Yoneda Y. Anomalous surface reflection of X-rays. Phys Rev. 1963;131:2010–3.